

Materials and Strategies to Enhance Melt Electrowriting Potential

Paula G. Saiz,* Ander Reizabal, Jose Luis Vilas-Vilela, Paul D. Dalton, and Senentxu Lanceros-Mendez

Melt electrowriting (MEW) is an emerging additive manufacturing (AM) technology that enables the precise deposition of continuous polymeric microfibers, allowing for the creation of high-resolution constructs. In recent years, MEW has undergone a revolution, with the introduction of active properties or additional functionalities through novel polymer processing strategies, the incorporation of functional fillers, postprocessing, or the combination with other techniques. While extensively explored in biomedical applications, MEW's potential in other fields remains untapped. Thus, this review explores MEW's characteristics from a materials science perspective, emphasizing the diverse range of materials and composites processed by this technique and their current and potential applications. Additionally, the prospects offered by postprinting processing techniques are explored, together with the synergy achieved by combining melt electrowriting with other manufacturing methods. By highlighting the untapped potentials of MEW, this review aims to inspire research groups across various fields to leverage this technology for innovative endeavors.

1. Introduction

In recent years, the convergence of innovative materials and advanced AM technologies has promoted a wave of transformative innovation with far-reaching implications.^[1] The capacity to fabricate intricate structures with tailored functionalities has disrupted various industries, encompassing medicine,^[2] electronics,^[3] or aerospace.^[4] By integrating new materials custom-tailored for these technologies, researchers, and engineers are pushing the boundaries of 3D fabrication, yielding personalized designs, programmed mechanical properties, and novel surface characteristics, among others. Within this landscape, various AM technologies have emerged, each wielding its unique strengths and weaknesses, charting the course for groundbreaking applications across diverse sectors.^[5]

Electrohydrodynamic (EHD) printing technologies have emerged as a promising solution for bridging the processability gap that often separates high-resolution printing methods from their large-scale, less precise counterparts.^[6] By harnessing electric forces to precisely control the deposition of materials, EHD printing technologies offer advantages for the fabrication of structures at the micro- and nanoscale, which can be further assembled to generate centimeter-scale structures.^[7] Among these EHD technologies, MEW stands out with its precise deposition of continuous polymeric microfibers into high porosity 3D structures.^[8] Since its discovery in 2011, a growing number of research publications and an increasing adoption of this technology by different labs worldwide have demonstrated the appeal of MEW.^[9] Of particular note is the recent surge in processing different materials via MEW, with a pronounced focus on endowing materials with functional properties, either intrinsic to the polymer (e.g., piezoelectricity or shape-memory) or achieved through the introduction of specific fillers and postprinting processes (e.g., magnetic responsiveness, conductivity, or fluorescence). This increasing trend on the use of MEW has been fueled by the growing number of research groups active in this field, the new functionalities introduced to the MEW devices, and the accessibility of the technique that has also played a pivotal role in its widespread adoption.

However, despite the growing interest, the exploration of MEW remains predominantly confined to specific domains,

P. G. Saiz, J. L. Vilas-Vilela
 Macromolecular Chemistry Research Group (LABQUIMAC)
 Department of Physical Chemistry
 Faculty of Science and Technology
 University of the Basque Country (UPV/EHU)
 Spain

E-mail: paula.gonzalez@ehu.es

P. G. Saiz, A. Reizabal, P. D. Dalton
 Phil and Penny Knight Campus for Accelerating Scientific Impact
 University of Oregon

1505 Franklin Boulevard, Eugene, OR 97403, USA

A. Reizabal, J. L. Vilas-Vilela, S. Lanceros-Mendez
 BCMaterials

Basque Center for Materials

Applications, and Nanostructures

Bldg. Martina Casiano, UPV/EHU Science Park


Barrio Sarriena s/n, Leioa 48940, Spain

S. Lanceros-Mendez

IKERBASQUE

Basque Foundation for Science

Plaza Euskadi 5, Bilbao 48009, Spain

 The ORCID identification number(s) for the author(s) of this article can be found under <https://doi.org/10.1002/adma.202312084>

© 2024 The Authors. Advanced Materials published by Wiley-VCH GmbH. This is an open access article under the terms of the [Creative Commons Attribution](https://creativecommons.org/licenses/by/4.0/) License, which permits use, distribution and reproduction in any medium, provided the original work is properly cited.

DOI: 10.1002/adma.202312084

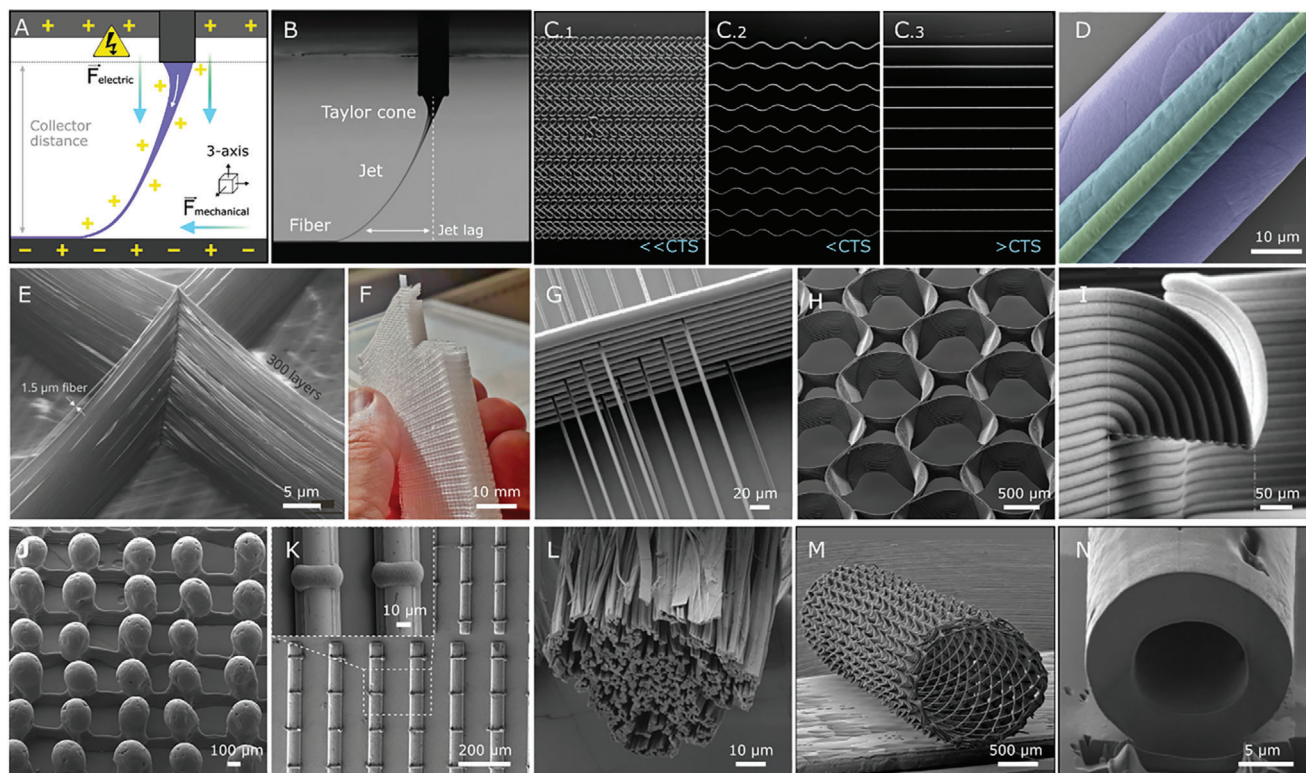


Figure 1. A) Schematic of the MEW working principle. B) Image of the MEW jet during the printing process above CTS. C) Coiling (C.1), sinusoidal (C.2), and straight (C.3) fibers printed at different velocities below and above the CTS. D) False-colored SEM images showcasing the fiber size control that MEW allows. E) Detail of 1.5 μm diameter fibers stacking into a 600 layers scaffold. F) 7.1 mm thick MEW scaffolds fabricated by adjusting the collector distance and voltage during printing. G) Suspended MEW fibers at different heights. H) MEW scaffold with circular pores made by combining sinusoidal deposited fibers. I) Overhangs allowing horizontal printing without supporting/sacrificial structure. J) Coalesced spheres observed for MEW of PVDF onto heated collectors. K) Poly(ϵ -caprolactone) (PCL) fragmented fibers. L) Detail of microfibril bundle obtained after dissolution of poly(vinyl alcohol) (PVAc) in a PVAc/PCL mixture scaffold. M) PCL tubular structure. N) Hollow fibers obtained with a coaxial nozzle. D) Reproduced with permission.^[19] Copyright 2018, Wiley-VCH. G) Reproduced with permission.^[20] Copyright 2021, Wiley-VCH. H, I) Reproduced with permission.^[21] Copyright 2020, Wiley-VCH. J) Reproduced with permission.^[22] Copyright 2021, Wiley-VCH. K) Reproduced with permission.^[23] Copyright 2022, Wiley-VCH. L) Reproduced with permission.^[24] Copyright 2021, Wiley-VCH. M) Reproduced with permission.^[25] Copyright 2018, Elsevier. N) Reproduced with permission.^[26] Copyright 2022, Wiley-VCH.

particularly within biomedicine, where it has found application in replicating the complexity of native tissues and stimulating their regeneration.^[10] Thus, its potential for innovation in new areas is yet to be fully explored and realized. To address this gap, this review aims to provide a comprehensive exploration of MEW technology's characteristics, and shed light on the possibilities it offers in terms of design freedom, new materials processing, and advanced functionalities. The aim is to further inspire and encourage research groups across diverse fields to harness the latent potential of this technology for their own endeavors. It is worth noting that this review is approached from a materials science perspective, highlighting the array of materials that have been processed, their applications, and specially, the main methods for enhancing MEW structures behavior and introducing novel functionalities, including fillers addition, postprinting processing, or combination with other techniques. Furthermore, it will shed light on areas where MEW has already found applications and potential areas of high interest such microfluidics, smart textiles, energy, or electronics. For a more exhaustive examination of the effects of printing parameters, we recommend

referring to a recent review that complements the aspects covered herein.^[11]

2. What is MEW?

MEW, earlier referred to as near-field melt electrospinning or melt electrospinning writing, is an EHD technology that enables the fabrication of high-resolution 3D porous macrostructures in a solvent-free mode. This innovative approach combines thermal energy and electrical forces, allowing for the controlled extrusion of molten polymers through a nozzle that subsequently forms well-ordered continuous micrometric fibers upon material solidification.

The basic configuration of MEW devices comprises several key components: a heated polymer feeding system, a three-axis positioning configuration that enables precise material deposition in three dimensions, and a high-voltage source capable of generating significant potential between the feeding system and a collector (**Figure 1A**). The feeding systems are typically based on either

pneumatically assisted syringe reservoirs or gear-assisted filament systems.^[12,13] Collectors exhibit greater variability and have been tested in various forms, including flat and static designs, cylindrical and dynamic configurations, spherical collectors, and other custom features tailored for specific applications.^[14,15] The electric field generated between the printhead and the collector induces charges on a molten drop, giving rise to the Taylor Cone as these charges overcome the surface tension of the molten material and the melt is jetted toward the collector (Figure 1B).^[16] A decrease in temperature facilitates the rapid solidification of the jetted material, resulting in the deposition of well-rounded fibers. The applied charges sufficiently minimize EHD instabilities so that the jet travels vertically toward the collector, allowing for precise control of its deposition by adjusting the relative positioning of the printhead. The relative traveling speed of the printhead (also referred as printing speed) plays a pivotal role in defining fiber morphology and shape. The jet speed can be determined by measuring the critical translation speed (CTS), at which the collected fiber becomes straight after buckling at lower speeds (Figure 1C.3).^[17] Below this CTS threshold, compression forces act on the jet as it impinges onto the surface, resulting in deposited fibers exhibiting a liquid rope coil effect (Figure 1C.1,C.2). Above CTS, the tension applied to the jet leads to a delay in the deposition point compared to the nozzle's position termed "jet lag" (Figure 1B). Consequently, jet lag results in material deposition that deviates from the desired pattern, causing defects in the final structure. To mitigate jet lag effects, one can either properly adjust printing parameters or employ predesigned patterns that account for the resulting shape variations.^[18]

Besides speed, fiber morphology is also influenced by other parameters, including printer setup (e.g., nozzle diameter, or nozzle to collector distance), processing conditions (e.g., applied voltage, applied pressure, or heating temperature), material properties (e.g., viscosity, electrical conductivity, or thermal stability), and environmental factors (e.g., ambient temperature and humidity).^[11] By fine-tuning these parameters, fiber size has been precisely controlled from 350 nm to 140 μm (Figure 1D).^[12,19]

MEW's remarkable capability to suppress Plateau–Rayleigh instabilities, coupled with the high viscosity and low conductivity of melt fluids, empowers precise control over very fine jets.^[27] By defining printhead relative movement, usually by computer numerical control languages (G-code), fiber placement can be readily controlled. This, combined with adjustments in other printing parameters (e.g., temperature, voltage, collector-head distance, etc.), enables the fabrication of high-resolution 3D porous structures in a layer-by-layer mode (Figure 1E). Nevertheless, due to charge accumulation in fibers, challenges remain regarding the maximum number of layers that can be stacked.^[28] Recent research endeavors, such as the work by Wunner and colleagues, have successfully achieved a 7.1 mm thick MEW structure through meticulous adjustments of voltage and working distance during the printing process to maintain a constant electrostatic force (Figure 1F).^[29]

Further, researchers are continuously pushing the boundaries of MEW by designing more complex structures, by carefully experimenting with the G-code, and optimizing the printing conditions to achieve precise control over fiber placement.^[21] While

early MEW designs were restricted to square-shaped boxes in a 0°/90° laydown pattern, researchers soon recognized the technology's potential for more intricate designs. By advanced programming and precise control over printing conditions different complex structures have been fabricated that include suspended fibers (Figure 1G), sinusoidal designs (Figure 1H), or tilted walls (Figure 1I), among others (Figure 1J–L). Microstructural design has demonstrated significant impact on aspects such as the mechanical properties or cellular behavior.^[30,31] Further, modifications to MEW devices have enabled the creation of more complex designs such tubular structures (Figure 1M) or hollow fibers (Figure 1N) through the use of rotating cylindrical collectors^[25] or coaxial nozzles,^[26] respectively. Additionally, the integration of other features like higher melting temperature, ultraviolet (UV) modules, or filament-driven systems have allowed to expand the range of processable materials.^[32,33] One of MEW's advantages lies in its ability to produce porous structures obtained when stacking these small microfibers, unlike electrospinning (ES), where excessive charges induce whipping instabilities that limit control over fiber placement and microstructural design.

Highly porous structures produced by MEW with biocompatible materials have found several applications in tissue engineering (TE), where the intricacy of structures plays a pivotal role in replicating native tissue complexity and supports bone, cartilage, skin, dental implants, and other tissue regeneration.^[34–37] Additionally, MEW's ability to process drug-loaded structures with controlled release properties have been demonstrated, providing another perspective that combines with the scaffold design possibilities.^[38,39] Many of the polymers processed by MEW so far have a history of clinical use, with poly(ε-caprolactone) (PCL) being the gold standard polymer used due to both its excellent processability and broad used within tissue engineering and regenerative medicine applications.^[40] All the biomedical applications of MEW have been described in detail in different reviews.^[10,41]

Despite its potential, MEW encounters some challenges that include scalability, accessibility, and materials processability, limitations that are being progressively solved. In this regard, machine learning algorithms have been implemented to better understand and optimize the printing process,^[42,43] multinozzle systems have been designed to increase productivity,^[44,45] and open-source, low-cost, and high-quality MEW devices have been developed to increase accessibility,^[12,32] fostering further research in the field. Further, in the past years there has been a notable surge in the range of materials processable by MEW, also with an emphasis on seeking functional and active properties in printed samples. Those properties may be inherent of the processed polymer, such as piezoelectricity, shape memory, or elasticity. Alternatively, they may be introduced through the processing of composites with functional fillers or by postprinting treatments to add extra functionalities like fluorescence, magnetism, or color-change capabilities. Overall, the processing of complex microstructures with functional responses is a key to extend the applicability of MEW in different areas. On the following, a comprehensive analysis of MEW materials and strategies for enhancing MEW structures' properties by fillers addition, postprinting processing or combination with other techniques is provided.

3. Polymers for MEW

Recent years have witnessed an expansion in the variety of polymers suitable for MEW, surpassing the landscape described in the review by Kade and Dalton just 2 years ago.^[46] The proliferation of processable polymers now exceeds three times the number previously reported on 2020, with a fourfold increase in the use of composite materials. This surge is expected to

continue, driven by enhanced accessibility to the technique, exemplified by open-source MEWron devices, and the incorporation of new functionalities into MEW printers, such as filament-based extrusion and higher processing temperatures.^[32] **Table 1** provides a comprehensive summary of these MEW-processed polymers, including printing conditions, resulting fiber sizes, microstructures, and their applications or most significant outcomes.

Table 1. Polymers printed by MEW together with the printing conditions and representative outcomes.

	Polymer	Printing conditions ^{a)}	Structure ^{b)}	Refs., Year
1 st steps – PCL	PCL	21G, 12 kV, 30 mm, 50 $\mu\text{L h}^{-1}$, 70 °C, 1000 mm min ⁻¹	Box, 50 layers, $\varnothing = 21 \mu\text{m}$	[9], 2011
	PCL	21G, 12 kV, 40 mm, 50 $\mu\text{L h}^{-1}$, 78 °C, 250 mm min ⁻¹	Tubes, $\varnothing = 60 \mu\text{m}$	[81], 2012
	PCL	22G, 4.25 kV, 3.5 mm, 120 kPa, 87 °C, 250 mm min ⁻¹	Circular paths, $\varnothing = 25 \mu\text{m}$	[21], 2020
	PCL	30G, 5.5 kV, 3 mm, 70 kPa, 75 °C	Box, 600 layers, = 1.5 μm	[32], 2023,
Toward new polymers	PCL/pHMGCL	27G, 5 kV, 3 mm, 200 kPa, 87 °C, 300 mm min ⁻¹	30 layers, $\varnothing = 5 \mu\text{m}$	[50], 2017
	PCL/PEG	45G, 2.3–2.6 kV, 1.5 mm, 1.5–3 kPa, 95 °C, 600–1200 mm min ⁻¹	15 layers, $\varnothing = 8 \mu\text{m}$	[38], 2020
	PCL/PVAc	–, 5 kV, 4 mm, 100–400 kPa, 165 °C	Fibrillar, $\varnothing = 0.25\text{--}1.5 \mu\text{m}$	[24], 2021
	PnPrOx/PcPrOx	–, 5 kV, 4 mm, 100–400 kPa, 225 °C	Fibrillar, $\varnothing = 0.25\text{--}1.5 \mu\text{m}$	
	PCL-PU	–, 4 kV, 6 mm, 60 kPa, 125 °C, 400 mm min ⁻¹	Single layer, $\varnothing = 15 \mu\text{m}$	[51], 2021
	PLLA	30G, 1.5–4 kV, 3 mm, 20–200 kPa, 190 °C, 57 °C, 1800 mm min ⁻¹	8 layers, $\varnothing = 30 \mu\text{m}$	[57], 2021
	PLLA	30G, 2.7 kV, 1.75 mm, 50 kPa, 184 °C, 75 °C, 960 mm min ⁻¹	Tubes, $\varnothing = 8 \mu\text{m}$	[60], 2024
	PLCL	23G, 6.5 kV, 5 mm, 35 kPa, 110 °C, 400 mm min ⁻¹	40 layers, $\varnothing = 26 \mu\text{m}$	[58], 2022
	PLGA	25G, 5.5 kV, 3.5 mm, 30 kPa, 145 °C, 600 mm min ⁻¹	Single layer, $\varnothing = 22 \mu\text{m}$	[59], 2022
	PLA/PEG	23G, 4 kV 3.5 mm, 200 kPa, 142 °C, 5000 mm min ⁻¹	5 layers, $\varnothing = 31 \mu\text{m}$	[56], 2017
UV treatment	PLA	28G, 2.8 kV, 2 mm, 180 kPa, 200 °C, 80 °C, 750 mm min ⁻¹	10 layers, $\varnothing = 30 \mu\text{m}$	[32], 2023
	p(LLA- <i>c</i> -CL-AC)	30G, 7 kV, 4.5 mm, 300 kPa, 130 °C, 400 mm min ⁻¹	100 μm spacing, $\varnothing = 25 \mu\text{m}$	[61], 2015
	p(<i>c</i> -CL-AC)	30G, 7 kV, 4.5 mm, 100 kPa, 50 °C, 300 mm min ⁻¹	10 layers, $\varnothing = 25 \mu\text{m}$	[62], 2018
	AUP mod. PCL	22G, 4.4 kV, 3.5 mm, 60 kPa, 89 °C, 707 mm min ⁻¹	Tube, $\varnothing = 17 \mu\text{m}$	[63], 2022
	Cinnamoyl- PCL	23G, 5–7 kV, 10 mm, 150 kPa, 60 °C, 4200 mm min ⁻¹	$\varnothing = 40^{\pm} \mu\text{m}$	[64], 2022
Water soluble	PETox	30G, 4 kV, 5 mm, 200 kPa, 210 °C, 400 mm min ⁻¹	30 layers, $\varnothing = 8 \mu\text{m}$	[52], 2014
	PEToxi	–, 2–4 kV, 150–200 kPa, 150 °C	10 layers, $\varnothing = 45 \mu\text{m}$	[65], 2020
	MeOzi-PentOx	23G, 3–4 kV, 4 mm, 100 kPa, 155 °C, 1500 mm min ⁻¹	20 layers, $\varnothing = 49 \mu\text{m}$	[39], 2023
	Isomalt	–, 5 kV, 2.5 mm, 200 kPa, 90 °C, 230 mm min ⁻¹	Single layer, $\varnothing = 30 \mu\text{m}$	[66], 2021
Mechanical prop.	PP	25G, 6.2 kV, 3.3 mm, 50–100 kPa, 215 °C, 80 °C, 750 mm min ⁻¹	10 layers, $\varnothing = 16 \mu\text{m}$	[67], 2017
	PUSi	24G, 10 kV, 8.5 mm, 200 kPa, 90 °C	100 layers, $\varnothing = 15 \mu\text{m}$	[68], 2018
	PEG-bisurea	22G, 4 kV, 2.2 mm, 100 kPa, 85 °C, 1000 mm min ⁻¹	20 layers, tube, $\varnothing = 66 \mu\text{m}$	[69], 2021
	TPU	–, 5 kV, 7 mm, 0.4 kPa, 220 °C, 12 mm min ⁻¹	4 layers, $\varnothing = 25 \mu\text{m}$	[73], 2022
	TPU	24G, 4 kV, 3 mm, 200 kPa, 220 °C, 50 °C, 450 mm min ⁻¹	6 layers, $\varnothing = 59 \mu\text{m}$	[32], 2023
Shape- memory	TPU PBA-75	27G, 3 kV, 2 mm, 100 kPa, 215 °C, 600 mm min ⁻¹	$\varnothing = 35 \mu\text{m}$	[74], 2022
	SMPU	25G, 3.3 kV, 5 mm, 25 kPa, 200 °C, 1500 mm min ⁻¹	$\varnothing = 58 \mu\text{m}$	[76], 2022
	LCE	25G, 10 kV, 30 mm, 15 kPa, 60 °C, 420 mm min ⁻¹ + UV crosslinking	50 layers, $\varnothing = 16 \mu\text{m}$	[33], 2022
Piezoelectric	PVDF	26G, 2.8 kV, 4 mm, 200 kPa, 190 °C, 4800 mm min ⁻¹	5 layers, $\varnothing = 30 \mu\text{m}$	[77], 2018
	PVDF	26G, 3 kV, 4 mm, 300 kPa, 190 °C, 110 °C, 4000 mm min ⁻¹	20 layers, $\varnothing = 40 \mu\text{m}$	[22], 2021
	PVDF-co-TrFE	22G, 3.7 kV, 4.4 mm, 50 kPa, 170 °C, 120 °C, 90 mm min ⁻¹	20 layers, $\varnothing = 10 \mu\text{m}$	[70], 2021
Filament based printing	PDO	400 μm , 4.5 kV, 4 mm, 32.5 $\mu\text{L h}^{-1}$, 135 °C, 600 mm min ⁻¹	Below CTS, $\varnothing = 20 \mu\text{m}$	[78], 2022
	PDO	250 μm , 3.5 kV, 2.6 mm, 1–18 $\mu\text{L h}^{-1}$, 115–140 °C, 70 °C, 450 mm min ⁻¹	FFF + MEW, $\varnothing = 20 \mu\text{m}$	[13], 2023
	PLA	200 μm , 3.5–4 kV, 5 mm, 600 $\mu\text{L h}^{-1}$, 230 °C, 60 °C, 3900 mm min ⁻¹	10 layers, $\varnothing = 15 \mu\text{m}$	[79], 2022
	PLA	150 μm , 3 kV, 1 mm, 33.7 $\mu\text{L h}^{-1}$, 160 °C, 90 °C, 350 mm min ⁻¹	4 layers, $\varnothing = 45 \mu\text{m}$	[32], 2023
	HDPE	150 μm , 3.5 kV 1.5 mm, 33.6 $\mu\text{L h}^{-1}$, 250 °C, 110 °C, 200 mm min ⁻¹	Auricular design, $\varnothing = 60 \mu\text{m}$	[71], 2023
Nylon 12	100 μm , 1.4 kV 1 mm, 16.8 $\mu\text{L h}^{-1}$, 230 °C, 150 °C, 100 mm min ⁻¹	Tubes, $\varnothing = 40 \mu\text{m}$	[72], 2023	

^{a)} Nozzle size, applied voltage, working distance, pressure/flow rate, printhead temperature, collector temperature (if applicable), speed; ^{b)} \varnothing = fiber diameter.

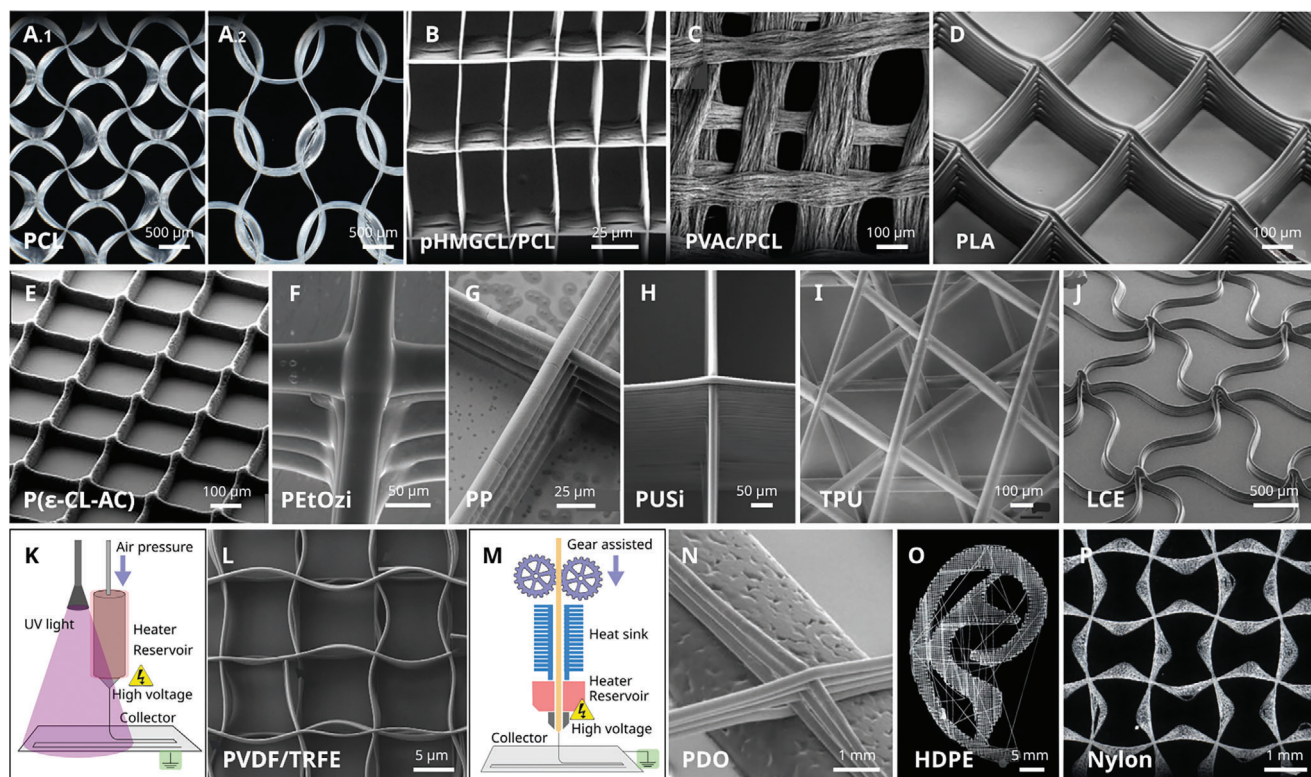


Figure 2. Some of the materials explored for MEW so far: A) Polycaprolactone (PCL). B) PCL/poly(hydroxymethylglycolide-*co-ε*-caprolactone) (pHMGCL) blends. C) PCL/poly(vinylacetate) (PVAc) blends after PVAc dissolution. D) poly(lactic acid) (PLA). E) poly(ϵ -caprolactone-*co*-acryloyl carbonate) (p(ϵ -CL-AC). F) poly(2-ethyl-2-oxazine) (PEtOzi). G) polypropylene (PP). H) poly(urea-siloxane) (PUSi). I) thermoplastic polyurethane (TPU). J) liquid crystal elastomers (LCE) processed with a: K) MEW device with incorporated UV lamp. L) Poly(vinylidene fluoride-*co*-trifluoroethylene) (PVDF-*co*-TrFE). M) filament-based MEW device that allows to print materials, such as: N) polydioxanone (PDO), O) high-density polyethylene (HDPE), or P) Nylon 12. A) Reproduced with permission.^[47] Copyright 2022, Wiley-VCH. B) Reproduced with permission.^[50] Copyright 2017, Wiley-VCH. C) Reproduced with permission.^[24] Copyright 2021, Wiley-VCH. D) Reproduced with permission.^[32] Copyright 2023, Elsevier. E) Reproduced with permission.^[62] Copyright 2018, Elsevier. F) Reproduced with permission.^[65] Copyright 2020, RSC Publishing. G) Reproduced with permission.^[67] Copyright 2017, Elsevier. H) Reproduced with permission.^[68] Copyright 2018, Wiley-VCH. I) Reproduced with permission.^[32] Copyright 2023, Elsevier. J) Reproduced with permission.^[33] Copyright 2023, Wiley-VCH. L) Reproduced with permission.^[70] Copyright 2021, Wiley-VCH. N) Reproduced with permission.^[13] Copyright 2021, Wiley-VCH. O) Reproduced with permission.^[71] Copyright 2023, Wiley-VCH. P) Reproduced with permission.^[72] Copyright 2023, Wiley-VCH.

When identifying MEW-compatible polymers, it is imperative to begin with poly(ϵ -caprolactone) (PCL), which is the polymer that dominates the field of MEW (Figure 2A).^[47] PCL boasts exceptional processability, primarily due to its low melting temperature (around 60 °C), thermal stability, high melt viscosity, and solidification dynamics. These attributes facilitate precise fiber deposition over extended durations while maintaining printing quality and avoiding thermal degradation.^[48] PCL's mechanical properties and biocompatibility makes it particularly suited for biomedical applications, and its degradability rate aligns perfectly with both the requirements of most 3D in vitro models and temporary implantable devices. This is why a substantial portion of MEW research has focused on the printing of PCL and, as a consequence, its processing parameters are well-established.

It is also notable that, medical-grade PCL processes better than its research or industrial-grade equivalent. In particular, medical-grade PCL from Corbion (PURASORB PC12) is the most frequently employed for MEW, known to yield excellent printing outcomes and with well-established printing conditions.^[48,49] However, other polymers including modified PCL, copolymers, and blends, have been extensively investi-

gated in the MEW realm.^[46] Most of the work in this direction attempted to modify the PCL original properties to tackle specific challenges. For instance, leveraging PCL's compatibility with other polymers, Castilho et al. explored the printing of poly(hydroxymethyl glycolide-*co-ε*-caprolactone) (pHMGCL) and pHMGCL/PCL blends.^[50] The hydroxyl-functionalized pHMGCL offered increased hydrophilicity, as well as possibilities for mechanical properties tuning, while maintaining print quality (Figure 2B). Further, pHMGCL/PCL blend scaffolds exhibited enhanced biocompatibility and improved cell retention and cardiac cell growth guidance capabilities. Directed also by the potential of MEW structures in biomedicine, Bay et al. delved into PCL/Polyethylene glycol (PEG) blends loaded with roxithromycin (ROX) for preventing and treat bone infection caused by implanted scaffolds.^[38] Composite materials processed at 95 °C resulted in well-ordered structures with up to 15 wt% of PEG and a fiber diameter as small as 8 μ m. PEG addition was found to enhance the hydrophilicity and the ROX release rates. In the realm of microstructural design, Ryma and colleagues explored the printing of PCL/poly(vinyl acetate) (PVAc) blends for design highly aligned microfibrillar bundles that mimic the 3D

topography of microfibrillar collagen.^[24] The blend was MEW-processed and subsequent dissolution of PVAc in ethanol resulted in fibrillary structures composed of 0.25 μm PCL constructs (Figure 2C). The increased surface area and bundles topography promote superior cell infiltration and induce pronounced elongation of human-monocyte-derived macrophages. Following the same strategy, they explored poly(2-*n*-propyl-2-oxazoline) (PnPrOx)/poly(2-cyclopropyl-2-oxazoline) (PcPrOx) processability, achieving also exceptional results in terms of processing and postprint fibrillation, leading to 1.5 μm fibrils bundles. Focusing on providing MEW scaffolds with additional functionalities, Uribe–Gomez and colleagues explored the printing of a PCL-polyurethane (PU) copolymer.^[51] Printed samples exhibited a good control over microstructure, with much rougher fiber surfaces than that observed for PCL. Furthermore, this material endowed MEW scaffolds with shape-changing capacities, opening new horizons for MEW applications.

While PCL and its copolymers and blends have been extensively investigated for MEW, the exploration of new materials is essential to expand the capabilities of this technique. Since the first report of MEW around 2011, PCL showed a prolonged dominance with no other materials processed until 2014.^[52] After that, progress in expanding the pool of MEW-compatible materials was initially slow (around 1 or 2 new materials introduced per year). This can be attributed in part to stringent material requirements, particularly in terms of thermal stability and melt viscosity, as MEW requires keeping materials in a molten state for extended periods. However, through advancements in devices and material design, the MEW material landscape is rapidly diversifying, with more than 40 materials, including polymers, copolymers, and composites, now processable by MEW, a number that keeps increasing due to a growing community working in the field.

Beyond PCL, poly(lactic acid) (PLA), and its copolymers and blends have been the second most explored materials for MEW, also due in part to its biomedical applications.^[53–56] Nevertheless, PLA and its copolymers' relatively poor thermal stability restricts their MEW processing at high temperatures for prolonged times. As an example, poly (*L*-lactic acid) (PLLA) can be processed by MEW at 190 °C with a heated collector at 57 °C.^[57] However, investigation of its processing windows revealed a reduced MEW printing time of ≈ 2 h and, in this period, a 10.8% reduction in viscosity was measured. In a similar approach, Reizabal and colleagues investigated the processing of PLA at 200 °C by reducing the time the melt is in the reservoir. This enabled good printing outcomes with stable fiber size of around 30 μm , fiber stacking of up to 10 layers, and negligible material degradation during the tested printing times (Figure 2D).^[32] Sanchez et al. explored the MEW processing of poly(*l*-lactide-*co*- ϵ -caprolactone) (PLCL), a copolymer of *L*-lactic (LA), and ϵ -caprolactone (CL), to modulate degradation and mechanical properties of the printed samples.^[58] High melt viscosity of PLCL initially hindered MEW processing at low temperatures, but thermal pretreatments at 150 °C for varying durations, ranging from 24 to 48 h, adjusted PLCL's molecular weight and consequently, reduced melt viscosity. This enabled MEW processing at lower temperatures (110 °C) while offering tunable degradability and mechanical performance, dependent on molecular weight. In a similar approach, Böhm and colleagues explored the processing of the

biodegradable poly(lactic-*co*-glycolic acid) (PLGA) copolymer.^[59] In this case, the processing temperature was increased to around 145 °C and an initial phase of printing instability with variable fiber diameters occurred due to thermal degradation. Stability was achieved after around 3.5 h of heating, resulting in homogeneous fibers over 24 h. Further, the addition of acetyl triethyl citrate (ATEC) enhanced samples elasticity and reduced PLGA processing temperature from 165 to 143 °C. More recently, Ashour and co-workers reported the successful processing, at around 180 °C, of high-quality PLLA scaffolds with up to 25 layers and different complex designs including tubular structures and auxetic structures.^[60] Interestingly, results suggest that drying the PLLA before printing can significantly restrain polymer degradation to extend the printing period to ≈ 1 day, opening new possibilities in the MEW field specially related to the higher rigidity of PLA compared to PCL.

Beyond PCL and PLA copolymers and mixtures, the post-processing UV treatment was found as an alternative for improving MEW outcomes mechanical properties. For example, Chen and colleagues investigated in 2015 the MEW processing of photocurable poly(*l*-lactide-*co*- ϵ -caprolactone-*co*-acryloyl carbonate) (p(LLA- ϵ -CL-AC)), demonstrating the possibilities for significantly increase the stiffness of the scaffolds (up to ≈ 10 -fold) after UV cross-linking, compared with not cross-linked samples.^[61] The processing temperature in this case was set to 130 °C and a thermally-stable photoinitiator was employed to avoid its degradation at the selected processing conditions. However, the material faced challenges related to stable fiber stacking and melt reservoir longevity at elevated temperatures. To address these issues, the same group explored another UV cross-linkable polymer, poly(ϵ -caprolactone-*co*-acryloyl carbonate) (p(ϵ -CL-AC)).^[62] In this case, the processing temperature was decreased to around 50 °C and the printing quality was considerably improved, compared to the p(LLA- ϵ -CL-AC), showing excellent stacking behavior and higher printing lifetime (Figure 2E). UV-curing post-processing resulted in a high tensile strength as well as in a considerable Young's modulus and elasticity increase. More recently, Pien et al. introduced photo-crosslinkable moieties to PCL by synthesizing an acrylate-encapped urethane-based polymer (AUP)-modified PCL.^[63] This material exhibited limited MEW processability but robust photo-crosslinking postprinting capabilities. To enhance printability, AUP-modified PCL was blended with commercial PCL, improving both printing behavior and mechanical properties through photo-crosslinking. Finally, Daneshfar and colleagues explored recently the processing of PCL functionalized with thermally stable and photo-dimerizing cinnamoyl groups.^[64] The thermal-stability of cinnamoyl groups enabled extended thermal processing while posterior UV curing improved thermo-mechanical properties. This modification yielded unique printing properties, including the emergence of spherulitic domains on printed fiber intersections, dependent on precursor polymer molecular weight and composition.

Water-soluble polymers have also garnered interest in MEW due to their suitability for creating specialized structures like channels and drug release designs, coupled with their biocompatibility. In 2014, Hochleitner et al. reported the successful fabrication of poly(2-ethyl-2-oxazoline) (PEtOx) microstructures. This turned out to be the second material processed by MEW, and fibers with diameters spanning 8–138 μm were produced

by adjusting processing parameters, including melting temperature within the 200–220 °C range.^[52] However, precise fiber stacking remained challenging, limiting the fabrication of ordered scaffolds. In a similar approach, Nahm and colleagues investigated the processing of hydrophilic poly(2-ethyl-2-oxazine) (PEtOzi) as an alternative to PEtOx, featuring a lower melting temperature.^[65] Processing temperature was reduced to ≈150 °C, yielding more accurate fiber stacking, and highly-ordered MEW structures with up to 10 well-stacked layers, featuring fibers of around 45 μm (Figure 2F). More recently, Keßler and colleagues investigated the processing of a poly(2-oxazoline)s (POx)-based amphiphilic triblock copolymer (MeOzi-PentOx-MeOzi) for developing a drug delivery system.^[39] Well-ordered structures with up to 20 stacked layers and fibers of around 49 μm were processed at 155 °C. Samples show a fast dissolution behavior in PBS media, suitable for drug release applications. Motivated also by its dissolution properties, Nadernezhad and colleagues investigated the MEW processing of Isomalt sugar for developing microfluidic channels.^[66] Isomalt was processed at 90 °C to achieve fibers with variable diameters in the 30 to 200 μm range depending on the applied pressure and voltage. Fast water solubility of Isomalt facilitated an easy fabrication of microchannels with on-demand control of channel size through MEW, opening intriguing possibilities for microfluidic applications.

While many reported MEW materials are biodegradable, the demand for nondegradable alternatives that introduce novel properties to MEW constructs motivated researchers to delve into a wider array of polymers, with particular emphasis on enhancing mechanical properties. For instance, Haigh and colleagues investigated the processing of polypropylene (PP), successfully demonstrating the production of high quality PP structures with up to 10 layers and fiber diameters as small as 16 μm (Figure 2G).^[67] Samples were processed at 215 °C, while simultaneously heating the collector to 70–80 °C. Notably, collector temperature resulted essential for achieving high-quality MEW processing of PP. Collector temperatures below 70 °C resulted in inadequate fiber adherence, while temperatures above 80 °C caused fiber melting and flattening due to slower polymer jet cooling. After this success, the elastic properties garnered attention, and elastomers MEW processing began. A good example is the work by Hochleitner and colleagues in which the MEW processing of a poly(urea-siloxane) (PUSi) segmented copolymer was investigated.^[68] This urea-siloxane copolymer consists of hard urea units and soft poly(dimethyl siloxane) (PDMS) segments to provide with a combination of thermoplastic and elastomeric properties. Printing conditions were investigated, showing that a continuous processing for up to 14 h was achievable at a moderate processing temperature of 90 °C, producing fibers with diameter as small as 15 μm and no noticeable degradation or pulsing. Interestingly, up to 50 layers could be stacked flawlessly, making it one of the polymers with the highest number of reported stacked layers after PCL, rendering it a highly promising option for MEW of more elastic materials (Figure 2H). Another example of segmented copolymers processing is given in the work by Mechau and colleagues in which the processing of a PEG-bisurea copolymer is investigated.^[69] Polymers with different molecular weights were processed to adjust the melt processing temperature. Their processing by different techniques (fused filament fabrication (FFF), MEW, and ES) was explored

in order to compare the printing outcomes. For MEW, polymers with higher molecular weights could not be processed even above 210 °C, due to thermal degradation, resulting in inhomogeneous printing outcomes, while those with lower molecular weights were successfully processed at 85 °C, producing uniform flattened fibers without any coiling or pulsing. Planar and tubular structures with up to 20 layers were printed, but the fibers exhibited a flattened morphology due to slow solidification and fiber merging after stacking. This effect led to an increase in fiber diameter up to 66 μm and limited microstructure design possibilities.

Thermoplastic polyurethanes (TPUs) have been also widely explored for MEW due to their mechanical properties. For example, Shao and colleagues investigated the MEW processing of hydrophobic TPU flexible meshes.^[73] Structures with up to 5 layers and fiber sizes around 25 μm were successfully designed by processing at 220 °C, although perfect layer stacking was not achieved. Beyond 5 layers, liquid-rope coiling effects were observed, resulting in disordered fibers. Fabricated meshes exhibited exceptional flexibility and elasticity, and were capable of returning to their original shape even after being folded. Furthermore, their potential to regulate breakthrough pressure by altering their microstructure (pore size and number of layers) was demonstrated. The control of microstructure enables the application of these structures for wearable sweat sensors. By leveraging the varying liquid permeability associated with different pore sizes, the sensor exhibits a delayed response to humidity sources, such as the sweat produced during physical activity. Finally, Reizabal and colleagues explored TPU processing using the MEWron open-source device to assess its capabilities for printing various polymers, especially those with high melting temperatures.^[32] Highly flexible structures with a fiber diameter of ≈59 μm were obtained by processing TPU at 220 °C while heating the collector to 50 °C, which likely improved fiber stacking and adhesion (Figure 2I).

The pursuit of novel applications for MEW has driven the investigation of materials with unique functionalities. A good example of this are shape memory polymers, offering the potential for 4D functionality (i.e., shape change) when exposed to specific stimuli. For instance, Constante and colleagues explored the processing of poly(1,4-butylene)-based poly(ester urethane) (TPU PBA-75) with shape memory properties.^[74,75] Fibers with diameters around 35 μm were achieved by adjusting processing conditions, with the melting temperature set to 215 °C. In this case, they focused on structures with straight parallel lines, examining how temperature influenced wetting properties, revealing that higher temperatures facilitated easier wettability due to the softness and deformability of the structure. Shape memory behavior of the structures after heating above the switching temperature (70 °C) and memory of mechanical properties was also demonstrated. The obtained smart structures with switchable/adaptive wetting properties have intriguing applications in areas, such as microfluidics for valve design or biotechnology for controlled drug release. In a similar approach, Costa and colleagues developed a shape memory hydrogel by embedding a commercially available shape memory polyurethane (SMPU) (DiAPLEX MM 3520, SMP Technologies Inc.) processed by MEW on them.^[76] Processing at 200 °C resulted in structures with fiber diameters of around 58 μm and excellent shape-memory abilities (100% shape-memory recovery

ratio above 37 °C). Driven further by the potential of controlling MEW constructs' mechanical response through external stimuli, Javadzadeh et al. processed via MEW liquid crystal elastomers (LCE) with temperature-responsive shape changes (Figure 2J).^[33] Interestingly, they incorporate for the first time UV light into the MEW device to enable direct crosslinking during the printing process, showcasing the potential of incorporating novel functionalities into MEW devices to enhance the technique's capabilities and expand the range of processable materials or improve printing outcomes (Figure 2K). LCE precursors mixed with a photoinitiator (Irgacure 369) were processed by MEW at 60 °C and subsequently cross-linked leading to different complex structures with fiber diameters as small as 16 μm, pore sizes as tiny as 90 μm and accurate stacking of up to 50 layers with perfect adhesion between them. The thermoresponsive behavior of LCE endowed fabricated structures with programmed temperature-triggered mechanical response, including fiber contraction, localized rotations, or pore-shape transformations. Overall, these studies highlight the potential of MEW in various fields, opening new avenues for developing smart structures for applications in soft robotics, microfluidics, and biomedicine, among others.

Another example of functional materials processed by MEW includes polyvinylidene fluoride (PVDF) and its copolymers, which are known for their piezoelectric behavior. First, Florczak and colleagues explored the printing of PVDF in 2018, demonstrating that high-temperature processing (190 °C) was possible.^[77] Well-ordered scaffolds with up to 5 layers and fibers with diameters of ≈30 μm were obtained under optimal processing conditions. Piezo-force microscopy confirmed the electroactive properties of the MEW-processed PVDF fibers, with d_{33} values around 19 pm V⁻¹ and an increased β-phase content compared to unprocessed material. However, the key limitation was structural design and handling, since the printing process becomes unstable above five layers and limited fiber fusion with lifting and warping of the printed structures toward the printhead was observed, limiting their applicability. In a more recent work, the same group investigated the effect of a heated collector during PVDF printing, demonstrating that better layer adhesion, reduced warping, and increased fiber stacking (up to 20 layers) could be achieved by heating the collector to around 110 °C.^[22] Additionally, an interesting phenomenon in which fiber intersection points coalesced into spheres of around 200 μm in diameter was observed when further increasing the collector temperature to around 150 °C (Figure 1J). Finally, this group also explored the MEW processing of electroactive poly(vinylidene fluoride-co-trifluoroethylene) (PVDF-co-TrFE) copolymer.^[70] Again, high melting (170 °C) and collector (120 °C) temperatures were required to achieve proper extrusion and ensure good fiber adhesion and stacking (up to 20 layers) with fiber diameters as small as 10 μm (Figure 2L). Interestingly, fibers exhibited high surface roughness with spherulitic or microfibrillar morphologies along them formed during the crystallization and solidification process. Finally, the β-phase content was demonstrated again to be higher than for the unprocessed material and dependent on the processing conditions. Overall, the main limitation for this material was thermal degradation, which limits the processing window to ≈5–10 h due to continuous heating at this elevated printing temperatures.

Thermal stability remains the key issue limiting the range of materials that can be processed using MEW. Recently, filament-driven MEW (F-MEW) systems have emerged as a promising solution to address thermal degradation (Figure 2M). In fact, it is interesting how different groups working in MEW recognized the potential of filament-driven systems, leading to the development of four different F-MEW devices within the past year. Systems were created by either modified existing FFF setups or entirely from scratch. The primary advantage of this filament-driven MEW devices over traditional milliliter volume syringe-based systems lies in significantly reducing the volume of material exposed to high temperatures down to around 50 μL. In syringe-based devices, the entire material volume (in the range of mL) remains molten at elevated temperatures above the material's melting temperatures throughout multihour and even multiday prints, which causes substantial thermal stress on the material, which can be especially detrimental for thermosensitive polymers. In contrast, F-MEW devices operate on a melt-on-demand principle similar to FFF devices, meaning that only a few μL of material remain molten for short times (in the range of minutes), resulting in considerably lower thermal stress. This characteristic enhances the feasibility of processing new materials, especially those with low thermal stability.

The first reported use of F-MEW was by Luposchinsky and colleagues at the end of 2022.^[78] They developed a homemade device mounted onto an optical breadboard, using the E3D Hemera 1.75 as the F-MEW printhead, and integrating it with a Meca500 robot arm to provide an extra level of freedom for working on nonplanar surfaces. In particular, a spherical collector was employed with the aim of designing dome structures by taking advantage of the six-axis robotic arm. This again highlights the significance of device design and the incorporation of novel functionalities to create more complex structures. The potential of the fabricated device was tested for poly(dioxanone) (PDO), a material previously unprocessed by MEW due to its low thermal stability. A temperature of 135 °C and a flow rate of 32.5 μL h⁻¹ were employed to process this material into dome structures with coiling fibers of around 20 μm in diameter. However, achieving straight fibers proved challenging due to limitations in robot speed, preventing printing above the CTS, and consequently precluding the stacking of successive layers. In a more recent approach, Mueller and co-workers also explored the F-MEW processing of PDO.^[13] In this instance, the F-MEW device was created by minimally modifying commercially available FFF printers (Prusa i3 MK3s+ and Kumovis HTRD1) to apply a high-voltage difference between the printhead and the collector. This allowed for easy conversion at a low cost, making F-MEW accessible to a wider community. For the conversion, an isolation ceramic plate with a metal sheet connected to the high-voltage above was employed as the print bed, while the nozzle was electrically grounded using a ring cable lug fixed between the hot end and the nozzle. The F-MEW device's performance was initially validated using PCL filament, yielding high quality printing outcomes, similar to that obtained by common syringe-based MEW devices, with fiber diameters as small as 10 μm for small flow rates of around 1.4 μL h⁻¹. Furthermore, much better outcomes were achieved for PDO filament compared to previous work, with straight fibers of around 20 μm in diameter as well as precise stacking of up to 5 layers when processing with a flow rate of

$10 \mu\text{L h}^{-1}$, with a melting temperature of 130°C and the collector heated at 70°C (Figure 2N). However, some thermal degradation of the PDO was still observed, resulting in a viscosity drop over time and occasional printing defects. To address this, the authors suggested shortening the heating block to reduce the reservoir volume and hence the time that the material remains heated in the reservoir below its degradation window. Notably, this device retained the capability to function in the FFF mode by simply switching off the voltage and reducing the working distance, allowing for dual-mode AM fabrication into a single device, further expanding the possibilities of the technique by combining large FFF structures with microstructure design provided by F-MEW.

In a similar approach, Shahverdi and colleagues also explored the modification of a commercial FFF device into a F-MEW device to extend the range of processable materials using MEW.^[79] In this case, heaters from the printhead were isolated using ceramic sleeves, while the bed was isolated using Kapton tape, making the modification process simple and cost-effective. The device was tested for PCL and PLA filaments, processed at melting temperatures of 100 and 230°C , respectively, with a flow rate of $\approx 600 \mu\text{L h}^{-1}$ and a collector temperature of 60°C . This resulted in fibers with diameters as small as 5 and $15 \mu\text{m}$ for PCL and PLA, respectively, and up to 5 stacked layers. However, high fiber pulsing and inaccurate stacking were observed, especially for the PLA. Authors attributed this effect to the use of Kapton tape to isolate the collector, which affects the electric field between the metallic nozzle and the substrate due to the electrical charge accumulation on the collector and fiber surface, leading to repulsive electric forces that hindered accurate placement. Eventually, the high flow rate employed in this work ($600 \mu\text{L h}^{-1}$) compared to the one order of magnitude lower values used in other studies may have contributed to the reduced printing quality. Furthermore, another critical consideration for those F-MEW devices is the discontinuous feeding of material into the reservoir due to the intermittent steps of the extruder motor at the low feed rates employed in MEW. This induces pressure pulses in the material reservoir and hence on the flow rate, resulting in variations in fiber diameter and a subsequent reduction in printing quality, which is a key issue to be solved.

Some of the previously described problems for F-MEW devices (charges accumulation in the collector, discontinuous polymer feeding, and high flow rates) have been successfully addressed in the filament MEWron device, a significant breakthrough reported recently by Reizabal and colleagues.^[32] As previously described, this innovative device is based on the conversion of an open-source Voron 0.1 printer into a versatile MEW device, capable of accommodating both syringe-based and filament-driven printing methods as well as other functionalities,^[80] achieving very good printing outcomes. In particular, for the F-MEW mode, several critical modifications that allow to improve the printing outcomes are introduced, including the modification of the gearbox system to enable the delivery of continuous and extremely low flow rates (around $10 \mu\text{L h}^{-1}$) and the incorporation of a borosilicate glass to insulate the heating components of the collector while maintaining a conductive top layer to prevent charge accumulation. Additionally, a ceramic head was designed to fully isolate the printhead. This comprehensive design allows for melting temperatures of up to 300°C and collector temperatures up to 150°C . The processing of PCL and PLA in

this F-MEW device was initially tested, yielding remarkably stable printing outcomes, especially for the PCL, with fiber sizes of around 25 and $45 \mu\text{m}$, and fiber stacking of up to 5 and 3 layers, respectively.

Further, by using this filament MEWron device the same group demonstrated recently the printing of other materials such as high-density polyethylene (HDPE) or Nylon 12, polymers that were unprocessable by MEW before due to their fast thermal degradation and high viscosity. In particular, Paxton and colleagues explored the processing of HDPE by F-MEW for manufacturing biomimetic auricular surgical implants (Figure 2O) due to the extended use of HDPE in this field.^[71] HDPE structures with a medium fiber size of $60 \mu\text{m}$ and fiber stacking of up to 5 layers were successfully achieved by processing at a melting temperature of 250°C , with the collector heated to 110°C to prevent fiber delamination, and applying a flow rate as low as $33.6 \mu\text{L h}^{-1}$. Moreover, they demonstrated the ability to optimize fiber diameters over a wide range by adjusting the extrusion feed rate. HDPE's thermal degradation at different temperatures was also investigated, revealing minimal mass loss during the processing window on the F-MEW device (≈ 30 – 60 min), in contrast to traditional syringe-based MEW devices with longer processing times and subsequent bigger mass losses. This underscores the critical role of F-MEW devices in processing materials like HDPE effectively. Interesting, fabricated HDPE scaffolds exhibited a remarkable 5.7-fold increase in ultimate tensile strength and a 13-fold increase in stiffness compared to conventional MEW PCL scaffolds, offering substantial opportunities for producing stronger and nondegradable scaffolds through MEW. As a case study, the MEW HDPE was successfully employed for fabricating patient-specific auricular surgical implants, unlocking numerous possibilities in this field. In another significant approach, Reizabal and colleagues also explored the processing of a high melting temperature polymer with fast thermal degradation, Nylon 12.^[72] Using the MEWron device, they successfully processed Nylon 12 microfibers of around $40 \mu\text{m}$ at a melting temperature of 230°C with the collector heated to 150°C and the flow rate set to $16.8 \mu\text{L h}^{-1}$. By carefully adjusting the printing parameters, complex microstructures were produced with sinusoidal fiber designs and up to 10 layers of stacking (Figure 2P). More importantly, this work introduced a novel modification to the MEWron device: the addition of a heated (up to 100°C) rotatory collector, reported for MEW for the first time. This innovation opens up new possibilities for designing MEW tubular structures using high melting temperature polymers. With the tubular collector indirectly heated at 100°C and a flow rate set to $16.8 \mu\text{L h}^{-1}$, the team successfully fabricated tubular structures of 2.5 mm in diameter with fibers of $\approx 60 \mu\text{m}$ in diameter, and up to 6 stacked layers with excellent adhesion between them. Importantly, Nylon 12 scaffolds exhibited also improved mechanical responses compared to PCL structures, with a 170% increase in ultimate tensile strength (UTS), 220% increase in elastic modulus, and 149% increase in yield strength, making fabricated structures highly promising for applications in different fields. It is important to note that all this reported work employs commercially available filaments, thus home-made filaments have not been tried yet, which should be the next step to evaluate, if variations on the home-made filament diameter led to printing defects due to small variations on the flow rate.

In conclusion, MEW has demonstrated remarkable progress in expanding the range of processable materials in the last years, a trend that continues due to increased accessibility to the technology and the introduction of novel functionalities such as filament-driven systems or photocuring modules. However, the application of these structures in different fields often requires additional functionalities, prompting the exploration of methods to enhance the potential of these structures. These methods include the addition of fillers, postprinting processing techniques, or combinations with other advanced manufacturing techniques, all of which will be discussed in the following sections.

4. Enhancing Melt Electrowritten Structures

The versatility to process a growing array of materials—ranging from enhanced elasticity, chemical stability, biodegradability, to piezoelectricity or even shape-memory properties—expands the horizons of MEW into various fields and applications. However, when aiming for specific functionalities or performances, polymers intrinsic properties can be limited, and thus it becomes imperative to provide MEW structures with novel functionalities. This can be achieved through the incorporation of functional fillers, postprocessing techniques, or by combining MEW with other structures into a multilayer/multitechnique approach. Each of these methodologies already employed for MEW are discussed in the following sections, together with their respective advantages, disadvantages, and potential applications.

4.1. Filler Addition

Incorporating functional fillers into a polymeric matrix to create a composite material, can enhance the material's original performance or even introduce novel functionalities. A wide range of fillers are commonly employed to develop composites, each one offering unique properties and functionalities. For instance, reinforcing fillers, can bolster mechanical strength, stiffness, and toughness; bioactive fillers, such as hydroxyapatite (HA) enable the modification of the biological response of materials, making them of great interest in the field of biomedical materials; other fillers such as magnetic or conductive particles, endow a matrix with novel properties such as magnetic response or conductivity, respectively. In the case of MEW, the use of fillers has witnessed substantial growth in recent years, but their impact on the printing process still deserves further research. Most important works describing the use of fillers in MEW are described in the following and summarized in **Table 2**. Additives to decrease the melting temperature or initiators have been already described above.^[33,59]

It is important to note that the incorporation of fillers can induce major changes in composite properties such as viscosity, melting temperature, crystallization dynamics, and structural integrity, thereby impacting the printability of the material and the final processed outcome. Additionally, fillers and their agglomerates have the potential to clog the nozzle and introduce defects larger than the extruded material's resolution. Hence, it is important to consider filler dimensions and dispersion to facilitate composite extrusion and good printing outcomes. Furthermore, fillers can influence the composite's conductivity, and given the

dependence of MEW on EHD forces, this can significantly affect material printability, processing conditions, and even the stacking behavior of fibers. Consequently, the careful selection of the appropriate filler and filler content, and the precise control of its dispersion, are of paramount importance to prevent printing defects. The most common strategy for fillers incorporation into a polymer matrix for MEW relies on the use of polymer solutions in which fillers can be easily dispersed by mechanical stirring, and subsequent solvent removal by evaporation (**Figure 3A.1**). Unfortunately, these processes require solvents, which can partially remain into the polymers, affecting their physical-chemical properties, processability, and performance. The use of twin-screw compounders can solve the problem by enabling components mixture and dispersion in melt (**Figure 3A.2**).

In general, fillers with good compatibility with the matrix will improve interphases in the composite, and will ensure good mechanical integrity. Likewise, nanoparticles will more effectively avoid nozzle clogging and printing accuracy defects. The addition of nonconductive fillers will allow maintaining a low melt conductivity, and thus the printing instabilities related with conductivity will be avoided. Finally, the use of inorganic fillers, or thermally stable organic compounds such as carbonaceous fillers, will ensure the composites properties stability during processing.

The majority of MEW research with fillers has employed PCL as the base polymer. This provides a common platform to analyze the specific effect of each filler on material properties, but also on the printing process. PCL is a broadly employed material for biomedicine due to its biocompatibility and degradability when placed within biological environments. PCL's limited bioactivity has been commonly addressed through coatings or fillers. Notably, HA has been widely explored for that purpose. For instance, Qu et al. employ HA nanoparticles to better mimic collagen fibers and HA crystals in natural bone.^[84] They successfully printed a PCL/HA composite containing 8 wt% of HA via MEW, yielding scaffolds with an average fiber diameter of 9 μm . While these composite scaffolds displayed excellent biocompatibility and supported cell proliferation and alignment, control over fiber stacking distance was limited due to a 100 μm minimum fiber spacing distance, which limits the design of structures using MEW. Similarly, Abdal-hay and colleagues explored the printing of PCL/HA composites via MEW at two different HA concentrations (3 and 7 wt%), comparing the results with bare PCL.^[82] This study yielded better control over fiber placement and stacking, with an increase in fiber roughness and diameter (from around 10 to 20 μm) as HA content increased from 0 to 7 wt%. SEM+EDX analysis confirmed the homogeneous distribution of HA particles along the fibers. Fabricated PCL/HA composite scaffolds promoted higher cell growth of human osteoblasts cells and exhibited a significant acceleration in degradation rates compared to bare PCL scaffolds (**Figure 3B**).

In a similar way, Hewitt et al. harnessed the potential of milk proteins (MP) to enhance the bioactivity of PCL scaffolds for skin regeneration purposes.^[85] In particular, they use lactoferrin and whey protein mixed independently with PCL at varying concentrations (0.05, 0.1, and 0.25% wt%), and together at 0.25 wt% each. It was observed that concentrations exceeding 1% could not be extruded from the MEW nozzle. Conversely, concentrations below 0.5 wt% resulted in increased material flow from the nozzle. The resulting MEW structures, featuring fiber diameter

Table 2. Composites processed by MEW together with the printing conditions and the effect of the filler on the outcome quality and on the overall functionality of the printed structure.

Filler	Matrix	Max. [wt%]	Printing conditions ^{a)}	Effect of fillers	Refs., Year
Hydroxyapatite (HA)	PCL	8	23G, 3 kV, 3 mm, 10 $\mu\text{L h}^{-1}$, 70 °C, 1800 mm min^{-1}	HA increase cell proliferation and alignment.	[84], 2016
		7	21G, 7 kV 10 mm, 20 mL h^{-1} , 80 °C	Increase on fiber diameter and roughness and higher cell growth and degradation rate.	[82], 2018
Milk proteins (MP)	PCL	0.5	25G, 20 kV 100 kPa, 85 °C, 720 mm min^{-1}	MP increase cell growth and infiltration, as well as degradation rates.	[85], 2019
Bioactive glass (BG)	PCL	0.75	25G, 7.5 kV, 6 mm, 280 kPa, 70 °C, 200 mm min^{-1}	BG enhances the wound healing of a gelatin hydrogel.	[86], 2022
	PLA/PEG	5	23G, 4 kV 3.5 mm, 200 kPa, 142 °C, 5000 mm min^{-1}	BG fibers are inhomogeneous in diameter and with some protuberances.	[56], 2017
Roxithromycin (ROX)	PCL/PEG	5	45G, 2.3–2.6 kV, 1.5 mm, 1.5–3 kPa, 95 °C, 600–1200 mm min^{-1}	ROX loaded scaffolds show antibacterial and drug release capacities as well as increased hydrophilicity.	[38], 2020
Indomethacin (IND)	MeOzi-PentOx copolymer	66	23G, 2.5–4.5 kV, 4 mm, 100 kPa, 130 °C, 700 mm min^{-1}	IND limits fiber stacking. Faster dissolution times for lower IND concentrations.	[39], 2023
NH ₂ -MIL-88B(Fe) MOF	PCL	20	23G, 5.4 kV, 5 mm, 300 kPa, 75 °C, 325 mm min^{-1}	Silver induced excellent antibacterial efficacy while the iron confers the scaffold with MRI capacities.	[88], 2023
Silver NPs (AgNPs)	PCL	3	27G, 3 kV, 4 mm, 200 kPa, 75 °C	AgNPs addition increases antibacterial activity but decrease mechanical properties.	[83], 2022
Magnesium phosphate (MgP)	PCL	20	23G, 7 kV, 3.5 mm, 80 kPa, 100 °C, 300 mm min^{-1}	MgP addition increased the tensile properties of PCL and promote better osteogenic differentiation of MSCs.	[90], 2023
Peptides	PCL	2	25G, 10 mm, 12 kPa, 95 °C, 600 mm min^{-1}	Peptides addition increases cell proliferation but printing quality become bad.	[101], 2023
Sodium titanate NWs & NTs	PCL	5	21G, 3–5 kV, 5 mm, 100–300 kPa, 90 °C, 100–900 mm min^{-1}	Ti/PCL composites show enhanced mechanical properties. Ti fillers should be functionalized to be printed.	[91], 2020
Reduced graphene oxide (rGO)	PCL	0.1	23G, 3.8 kV 250 kPa, 90 °C, –	rGO improves mechanical properties in tubular structures.	[92], 2020
Graphene	PCL	0.5	25G, 5 kV, 4.8 mm, 10 kPa, 100 °C, 3300 mm min^{-1}	Graphene decreases degradation rate and significantly improve the tensile strength.	[93], 2022
Graphene nanoplatelets	PCL	10	27G, 6 kV, 4 mm, 200 kPa, 105 °C, 240 mm/min	Composite samples show bending under different magnetic fields and similar cell viability to PCL after several days in culture.	[99], 2023
Multiwalled carbon nanotubes (MWCNT)	PCL	0.2	5 kV, 4 mm, 30 $\mu\text{L h}^{-1}$, 70 °C, 2400 mm min^{-1}	MWCNTs addition promotes a decrease on the impedance while mechanical properties are not affected.	[94], 2020
Fluorescent nanodiamonds (FNDs)	PCL	0.1	23G, 6 kV 4 mm, 0.15–17 kPa, 100 °C, 250 mm min^{-1}	FNDs allow for real-time tracking of degradation and increase cell proliferation.	[95], 2023
Ultrasmall superparamagnetic iron oxide particles (USPIO)	PCL	0.3	23G, 5 kV, 3.1 mm, 200 kPa, 85 °C, 360 mm min^{-1}	USPIO served as contrast agents to obtain MRI detectable MEW scaffolds.	[96], 2021
Thermochromic dyes	PCL	4	24G, 6.3 kV, 3.5 mm, 240 kPa, 80 °C, 260–460 mm min^{-1}	Samples respond to temperature by changing the color at specific temperatures.	[97], 2023
Carbonyl iron (CI) particles	PVDF	30	26G, 3 kV, 2.5 mm, 300 kPa, 200 °C, 2800 mm min^{-1}	Composite samples demonstrate magnetic response and similar cell adherence and viability to pure PVDF.	[98], 2022
Iron-oxide nanoparticles (Fe ₃ O ₄ NPs)	PCL	10	25G, 4.8 kV, 3 mm, 150 kPa, 90 °C, 400 mm min^{-1}	Different designs allow controlled magnetic responses (grip, preferential orientation, etc.).	[100], 2023

^{a)} Nozzle size, applied voltage, working distance, pressure/flow rate, printhead temperature, speed. –: Not reported.

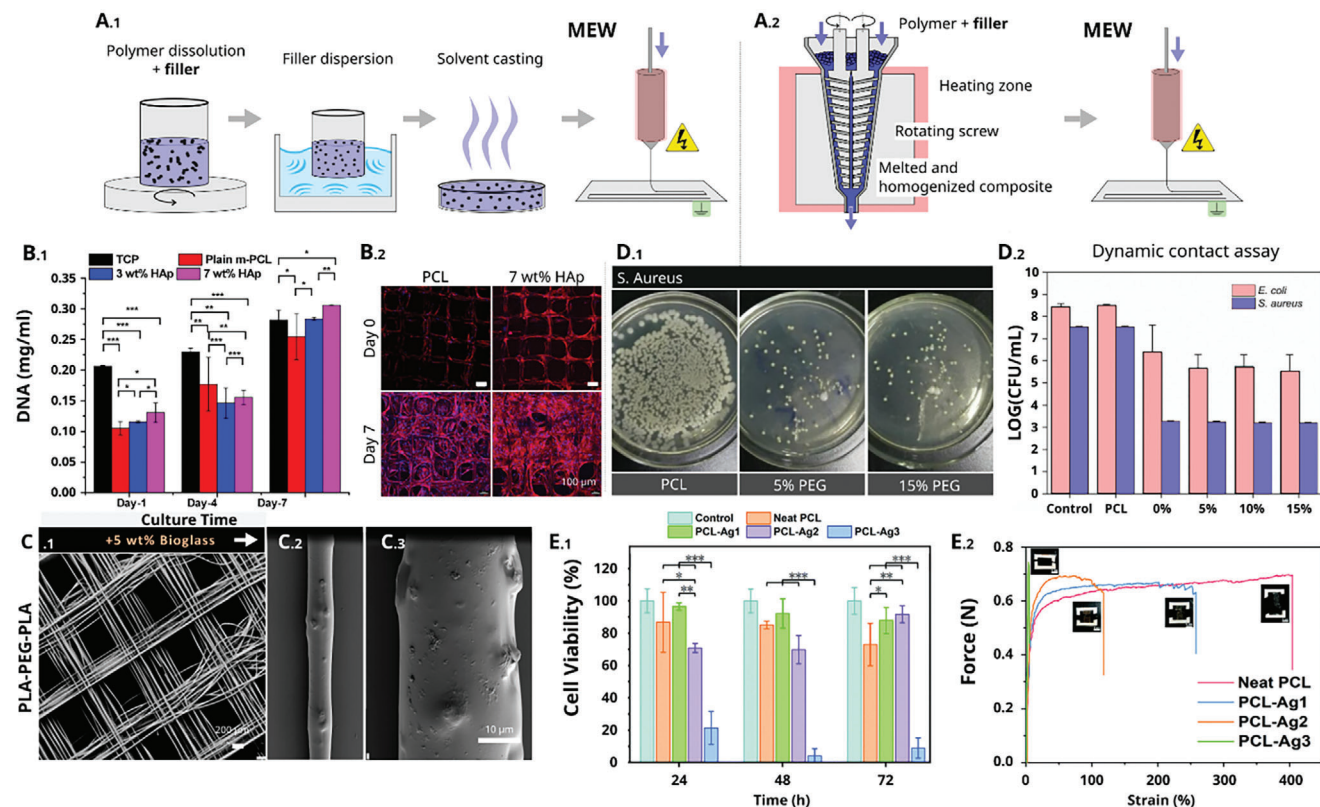


Figure 3. A) Graphical representation of commonly used experimental procedures for incorporating fillers into MEW processable polymers: A.1) Multi-step solution-based mixture, A.2) Single-step twin-screw compounder-based mixture. B) Human osteoblast cells adhesion on PCL and PCL/HAP composite scaffolds as a function of culture time: B.1) DNA estimation (PicoGreen assay). B.2) Cell morphology and cell spreading over 7 days of culture. C) SEM overview of: C.1) PLA-PEG-PLA scaffolds. C.2-3) PLA-PEG-PLA fibers with 5 wt% of bioglass. D) Antibacterial activity of 5 wt% ROX-loaded PCL scaffolds with different PEG content: D.1) Agar plates of *S. aureus* suspensions treated with the scaffolds. D.2) Calculated log (CFU) against *E. coli* and *S. aureus*. E) Effect of Ag NPs addition on PCL scaffolds: E.1) Cell viability of L929 cells after culturing for 24, 48, and 72 h on PCL scaffolds with varying Ag NPs concentrations. E.2) Tensile tests of neat PCL and PCL/AgNP composite scaffolds (inset: pictures of the samples after fracture). B) Reproduced with permission.^[82] Copyright 2018, Elsevier. C) Reproduced with permission.^[56] Copyright 2017, Elsevier. D) Reproduced with permission.^[38] Copyright 2020, Elsevier. E) Reproduced with permission.^[83] Copyright 2022, RSC Publishing.

around 50 μm , exhibited no significant differences when compared to bare PCL structures. However, the presence of MP led to increased swelling ratios, particularly in samples combining both proteins, and also exhibited faster degradation. Most significantly, MP presence substantially increased cell growth, spreading, and infiltration, particularly for samples containing 0.25 wt% of lactoferrin and those with a combination of both proteins.

Another compound explored to increase the bioactivity of PCL scaffolds is bioactive glass (BG). For instance, Afghah et al. employed PCL/BG composite MEW scaffolds as a reinforcement matrix within a gelatin hydrogel to significantly improve wound healing rates of the hydrogel.^[86] Fibers of around 80 μm in diameter with an increase in surface roughness were successfully processed by MEW with 0.75 wt% of BG. This small concentration of BG was sufficient to confer the hydrogel with the desired properties. Paxton et al. further extended this concept by investigating the printing of strontium-substituted BG (SrBG)/PCL composites with 33 wt% of SrBG.^[87] However, they found that this composite was unprintable via MEW due to rheological properties that hindered extrusion. To overcome this, they employed a solvent to lower the sample's viscosity, enabling the printing of or-

dered structures via solution electrowriting. This highlights the advantage of combining a highly viscous melt containing a high particle content with a solvent to process materials that are otherwise unprintable with MEW. Although it introduces an extra variable to the process, requires additional equipment, and can result in solvent traces in the final material.^[6] Finally, Hochleitner and colleagues also explored the use of BG but in this case using a PLA/PEG blend as the polymer matrix (Figure 3C).^[56] They incorporate a 5 wt% of BG and were able to obtain straight ordered fibers of around 31 μm in diameter with a rough surface in which some protuberances and particles agglomerations along the surface could be observed.

Continuing the exploration of bioactive fillers potential related to MEW processing, Bai et al. investigated the printing of PCL/PEG blends combined with roxithromycin (ROX).^[38] For that, the concentration of PEG was varied from 0% to 15%, while ROX concentration remained constant at 5 wt%. Highly ordered scaffolds with up to 15 well-stacked layers and fiber diameters around 8 μm were successfully obtained for all samples. The addition of both PEG and ROX improved the hydrophilicity of the scaffolds, evidenced by a decrease in contact angle with

increasing PEG content. Cell viability analysis indicated that ROX-loaded scaffolds retained cell viability and growth capacities. Antibacterial efficiency was also investigated, demonstrating strong antibacterial activity against *E. coli* and *S. aureus* for all the drug-loaded scaffolds compared to pure PCL scaffolds (Figure 3D). Additionally, ROX release studies showed that the presence of PEG resulted in an improved drug release rate, attributed to the enhanced hydrophilicity of those scaffolds. Continuing the realm of drug delivery, Kessler and colleagues explored the incorporation of indomethacin (IND) anti-inflammatory drug onto poly(2-oxazoline)-based amphiphilic triblock copolymer for subsequent MEW processing.^[39] Different IND concentrations ranging from 0 to 66 wt% were investigated. By adjusting printing conditions, highly ordered structures were obtained, with varying fiber sizes, depending on IND concentration (36±12 μm for the 66 wt% samples). However, after 5–10 layers printing, fiber pulsing was observed for the IND-loaded scaffolds, limiting extensive fiber stacking, and processing temperatures result in material degradation after several printing hours. Dissolution behavior tests further show drug loading-dependent dissolution behavior, being those samples with larger IND concentration the ones with slower dissolution profile.

With the focus on antibacterial properties, Mansi and co-workers explored recently the incorporation of silver-decorated iron-based MOFs (NH₂-MIL-88B(Fe)).^[88] High-quality scaffolds with up to 20 wt% of MOF were successfully fabricated with a medium fiber diameter of 50 μm. Among these, 10 and 20 wt% samples showed a cell viability below 70% thus 5 wt% of MOF results the optimal concentration as it already exhibits silver-induced excellent antibacterial efficacy while maintaining PCL cytocompatibility. Giving a step forward, the iron nodes of the MOF confers the scaffold with magnetic resonance imaging (MRI) capabilities, thereby enabling noninvasively scaffold monitoring upon implantation. Focus also on antibacterial properties, Du and colleagues investigated the use of silver nanoparticles (AgNPs) embedded onto PCL MEW scaffolds to improve antibacterial activity.^[83] AgNPs were employed to avoid the use of antibiotics which can promote drug-resistance and reduce efficacy. Different AgNPs concentrations of 1, 2, and 3 wt% were explored. Ordered scaffolds with up to 20 well-stacked layers and medium fiber diameter of 13 μm were obtained regardless of NPs concentration. Bactericidal activity of these MEW lattices was investigated, revealing a direct correlation between AgNPs concentration and antibacterial efficacy, achieving 100% and 96.96% antibacterial ability against *E. coli* and *S. aureus*, respectively, for the samples containing 2 wt% of AgNPs. Cytotoxicity analysis showcases a cell viability of more than 70% for the 2 wt% samples, while reduced activity was observed for the 3 wt% samples (Figure 3E.1). Further, the addition of AgNPs resulted in decreased mechanical properties, with a reduction in elongation to break from 402% for the pure PCL to 258% for samples with 1 wt% of NPs and just 4% for the 3 wt% samples, which could be detrimental for some applications (Figure 3E.2).

Mechanical properties are a critical aspect when designing structures for various applications. As previously discussed, by modifying the microstructure design or the material itself, different researchers have successfully tuned the mechanical properties of MEW scaffolds.^[89] Another potential approach to increase the mechanical properties of MEW scaffolds is the ad-

dition of reinforcement fillers. One example of this was introduced by Golafshan et al. who introduced magnesium phosphate (MgP) particles to improve the mechanical properties of PCL scaffolds.^[90] MgP bioceramics were chosen due to their known ability to promote bone regeneration. Samples containing 0, 10, and 20 wt% of MgP, were successfully processed with a total of 10 well-stacked layers featuring diameters ranging from 20 to 50 μm. The addition of MgP significantly enhanced the tensile properties of PCL, resulting in a threefold increase in tensile modulus when 20 wt% MgP was incorporated (Figure 4A.1). Additionally, MgP composites exhibited enhanced osteogenic differentiation of mesenchymal stem cells compared to pure PCL and simultaneous in vivo scaffold degradation (Figure 4A.2). Also with the aim to improve the PCL mechanical properties, Pang and colleagues explored the use of sodium titanate nanofillers with different aspect ratios.^[91] In particular, they employ both nanowires (NWs) and nanotubes (NTs) at concentrations ranging from 0.5 to 5 wt%. Besides, they investigated the functionalization of nanofiller surfaces with two different functional groups (phenyl- and thiol-terminated ligands). Functionalization, improved filler dispersion in PCL matrix, and enabled composites printing, which were otherwise unprintable without functionalization (Figure 4B.1). This approach resulted in the successful printing of straight fibers around 34 μm in diameter, although no fiber stacking or additional designs were investigated. The sodium titanate/PCL films exhibited enhanced mechanical properties, with a Young's modulus of 1.67 GPa, almost 8 times higher than that of pristine PCL (0.22 GPa) (Figure 4B.2).

In a similar approach, Somszor et al. explored the use of reduced graphene oxide (rGO) to improve the mechanical properties of stent-like tubular constructs fabricated via MEW.^[92] PCL composites with different rGO concentrations ranging from 0.1 to 1 wt% were investigated, finding that the 0.1 wt% sample provided the most consistent and reproducible MEW printability. For that sample, different complex tubular structures with well stacked layers and fibers of around 60 μm in diameter were successfully printed (Figure 4C). PCL/rGO structures exhibited superior mechanical properties compared to bare PCL, with a 2.5-fold increase in Young's modulus and a 1.5-fold increase in ultimate tensile strength. Chung and colleagues also investigated the effect of graphene additives on PCL scaffolds.^[93] Samples containing 0.1 and 0.5 wt% graphene with a medium fiber size as small as 16 μm were successfully printed by adjusting the printing conditions. Printing was not feasible above these concentrations due to viscosity increasing. The presence of graphene decreased the samples' degradation rate, and most importantly, it significantly increased the tensile strength by more than 270% compared to pristine PCL (Figure 4D). In a similar approach, Meng et al. explored the impact of multiwalled carbon nanotubes (MWCNT) on the overall printability and mechanical properties.^[94] The addition of MWCNT in PCL at very low concentrations (0.2 wt%) had little effect on the stability of melt-based EHD printing, obtaining samples with good fiber stacking for up to 20 layers and fibers with diameters of 18 μm. The obtained composite scaffolds possessed mechanical properties similar to that of pure PCL scaffolds but exhibited a significant decrease in impedance. Interestingly, a maximum of 0.2 wt% of MWCNTs was used in the study, suggesting that higher concentrations may interfere with the printing process due to material's

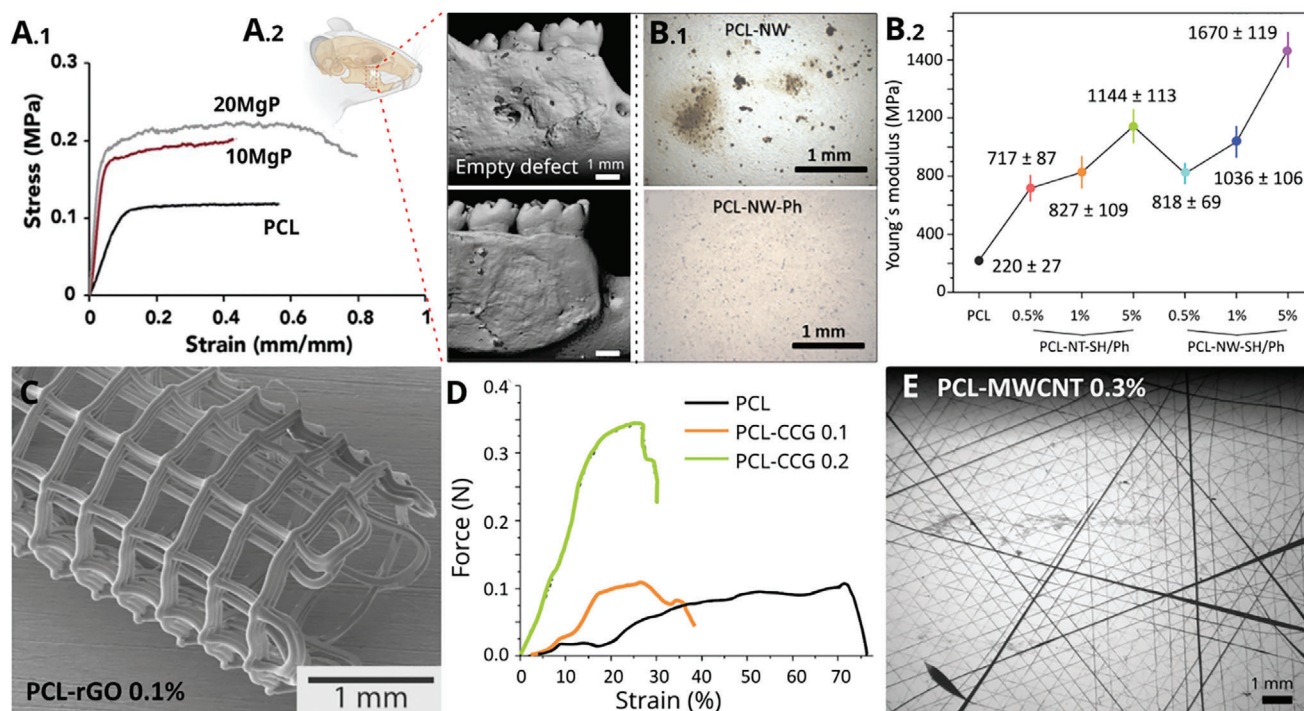


Figure 4. A) Effect of MgP addition on PCL scaffolds: A.1) Representative stress–strain curves of MEW scaffolds with different MgP concentrations. A.2) Microcomputed tomography (μ CT) images of the fenestration defect exposing the distal root of the second molar at 6 weeks. B) Effect of sodium titanate nanofillers functionalization on their dispersion on a PCL matrix: B.1) Optical images of PCL films mixed with nonfunctionalized and functionalized sodium titanate nanofillers. B.2) Average Young's modulus of PCL films with different sodium titanate nanofiller concentrations and aspect ratio. C) SEM images of PCL-rGO 0.1% stent-like structure produced via MEW. D) Stress–strain curves of PCL/graphene composites. E) Representative printing defects on a PCL/MWCNT composite with 0.3 wt%. A) Reproduced with permission.^[90] Copyright 2022, ACS publications. B) Reproduced with permission.^[91] Copyright 2020, ACS publications. C) Reproduced with permission.^[92] Copyright 2020, ACS publications. D) Reproduced with permission.^[93] Copyright 2022, MDPI.

increased electrical conductivity. This interference added an extra layer of complexity to the printing process and usually results in printing defects, such as jet breaking and pulsing, as can be shown in Figure 4E for a PCL/MWCNT composite containing just 0.3 wt% of MWCNTs.

Research has also shifted from improving existing functionalities to introducing novel active responses into MEW-printed samples, such as magnetic response or imaging capabilities through functional fillers, in order to extend the applicability of MEW. Representative examples include the use of nanoparticles for scaffolds noninvasive imaging, or dyes for temperature-responsive color-change scaffolds development. To achieve fluorescence, Wu et al. employed biocompatible fluorescent nanodiamonds (FNDs) with a concentration of up to 0.1 wt% to enable fluorescence-based tracking imaging in MEW PCL scaffolds.^[95] Printed samples exhibited excellent quality with up to 4 well-stacked layers and an average fiber size of around 20 μ m (Figure 5A.1). The addition of FNDs increased the tensile modulus by 1.25-fold and led to improved cell proliferation and slower degradation compared to pure PCL (Figure 5A.2). Importantly, even a very low concentration of FNDs (0.001 wt%) allowed for real-time tracking of scaffold degradation by confocal microscopy (Figure 5A.3). Ultrasmall superparamagnetic iron oxide (USPIO) nanoparticles have been employed by Mueller et al. for a similar purpose.^[96] Samples containing up to 0.3 wt% of USPIO were

successfully processed into highly ordered MEW microstructures with fibers of around 33 μ m in diameter (Figure 5B.1). Mechanical and cytocompatibility evaluations indicated that USPIO particles had minimal impact on these properties, making the functionalized PCL scaffolds still suitable for biomedical applications. Further, the USPIO particles served as contrast agents achieving MRI-detectable MEW scaffolds, potentially enabling noninvasive monitoring of implant functionality (Figure 5B.2). In a different study, the work by Saiz and colleagues focused on introducing temperature-responsive dyes into MEW scaffolds for thermochromic scaffolds development.^[97] Different concentrations ranging from 0 to 6 wt% were investigated showing that up to 4 wt% of fillers allowed successful printing outcomes with good fiber stacking of up to 5 layers and quite small fiber diameters of 20 μ m (Figure 5C.1). Fabricated scaffolds exhibited a characteristic black color that further changed to pink when heating above 35 $^{\circ}$ C. Additionally, multimaterial structures combining layers with different thermochromic dyes were explored, demonstrating distinct color changes at different temperatures (Figure 5C.2). Such active structures hold promise for different applications, especially when precise microstructure design control is required.

Magnetic fillers are also a highly interesting class of filler due to their inherent response to noninvasive magnetic fields. This is probably one of the main reasons why different authors have investigated the printing of magnetic composites by MEW in

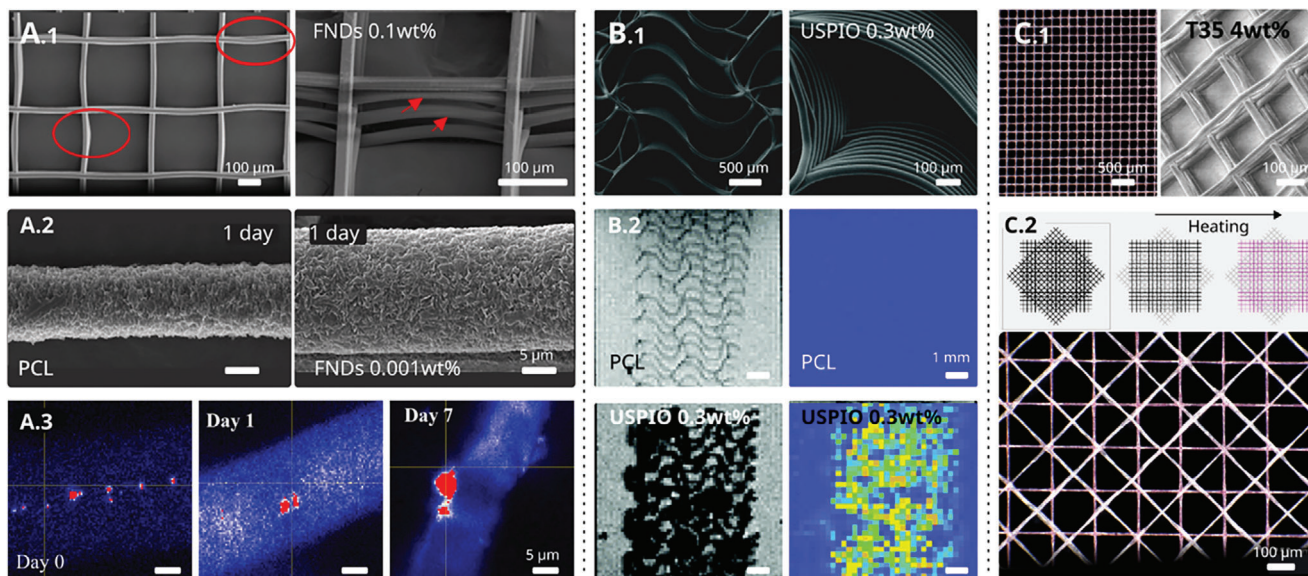


Figure 5. Detail of composite scaffolds printing with fillers that provide the samples with imaging or visual responses: A) Fluorescent nanodiamonds addition to PCL scaffolds: A.1) SEM images of MEW PCL-FND 0.1 wt% mesh (Red circles and arrows showcase printing defects as consequence of filler addition). A.2) SEM images showing the PCL versus PCL-FND 0.1 wt% fiber degradation in enzymatic solution after 1 day. A.3) Fluorescent images tracking the degradation of PCL-FND 0.1 wt% scaffolds after 0 h, 1 day, and 7-day of enzymatic degradation (Nanodiamonds are shown in red and autofluorescence from fibers is shown in blue). B) USPIO nanoparticles addition to PCL scaffolds. B.1) Morphological characterization of PCL with 0.3 wt% of USPIO. B.2) MRI visualization and R2* map of PCL and PCL/USPIO scaffolds embedded in agar-agar. C) Thermochromic dyes addition to PCL scaffolds: C.1) Digital microscope and SEM images of PCL meshes containing 4 wt% of T35 thermochromic dye. C.2) Scheme and digital microscope images of multimaterial structure combining layers with different thermochromic dyes. A) Reproduced with permission.^[95] Copyright 2023, Elsevier. B) Reproduced with permission.^[96] Copyright 2021, Wiley-VCH. C) Reproduced with permission.^[97] Copyright 2023, ACS publications.

recent years. One example is the work of Kade and colleagues, in which the addition of carbonyl iron (CI) particles into PVDF MEW structures is explored.^[98] Remarkably, this work demonstrated successful printing with up to 30 wt% filler in a PVDF matrix (Figure 6A.1). A decrease of the printing quality is observed as the amount of fillers increase, with a less accurate placement of fibers and rougher surfaces being observed especially for the 30 wt% samples. The filler addition considerably influenced the melt viscosity, thus affecting the printing process (Figure 6A.2). Overall, EDX results demonstrate a homogeneous distribution of the particles along the fibers, despite some agglomerations can be observed (Figure 6A.3). The fibers show an average diameter of 40 μm for all the printed samples, although the fiber size becomes more variable as the amount of particles increases. Notably, fibers can be readily displaced using magnets at concentrations as low as 1 wt%, opening possibilities for magneto-active stimulation or actuators. Finally, cell viability test indicated that samples with up to 30 wt% of CI showed similar cell adherence and viability to pure PVDF (97% for pure PVDF versus 80% for the 30 wt% sample), suggesting potential applications of the fabricated scaffolds for magneto-active cell stimulation.

In a similar approach, Cedillo-Servin and colleagues proposed the use of magneto-active scaffolds for remote stimulation of 3D *in vitro* skeletal muscle models.^[99] In this case, oxidized graphene nanoplatelets functionalized with iron oxide (rGNP@) were employed as fillers in a PCL matrix, and samples with 0, 2, and 10 wt% of rGNP@ were successfully processed by MEW, though a decrease in the printing quality was observed as the amount of filler increased. All samples exhibited a similar fiber

size of 20 μm , which was further tuned by adjusting the printing conditions. Magnetic scaffolds displayed bending behavior under different magnetic field intensities, which further depend on the filler concentration. Cell viability experiments indicated initial lower cell viability for magnetic structures that returned to normal behavior after several days, suggesting again suitability for dynamic culture and remote magnetic stimulation.

In a more active-response focused approach, Saiz et al. explored the possibilities of microstructure design offered by MEW combined with the possibilities of magnetic fillers to create complex structures with tailored magnetic responses.^[100] In this case, iron-oxide nanoparticles (Fe_3O_4 NPs) were employed, to favor filler dispersion along the matrix, and PCL as the polymer matrix to ensure a low melting temperature and good printing outcomes. High-quality structures with fiber diameters around 10 μm were successfully processed with up to 5 wt% of NPs, while jet break and particle agglomeration were observed above 10 wt% (Figure 6B.1). Samples with 1 and 5 wt% of NPs were further processed in different complex geometries, including cross-shaped macrostructures, butterflies, and gradual tubular microstructures, to investigate the possibilities for magnetic response control by microstructure design (Figure 6B.2). These constructs exhibited responses such as grip, wing movement, or preferential orientation of tubes, depending on the design and nanoparticle content (Figure 6B.3). In a step forward, multimaterial structures were designed which allow the magnetic response in just some parts of the structures (Figure 6B.4). Overall, those results demonstrate the potentials of MEW in the field of 4D printing for microstructure design and programmed response.

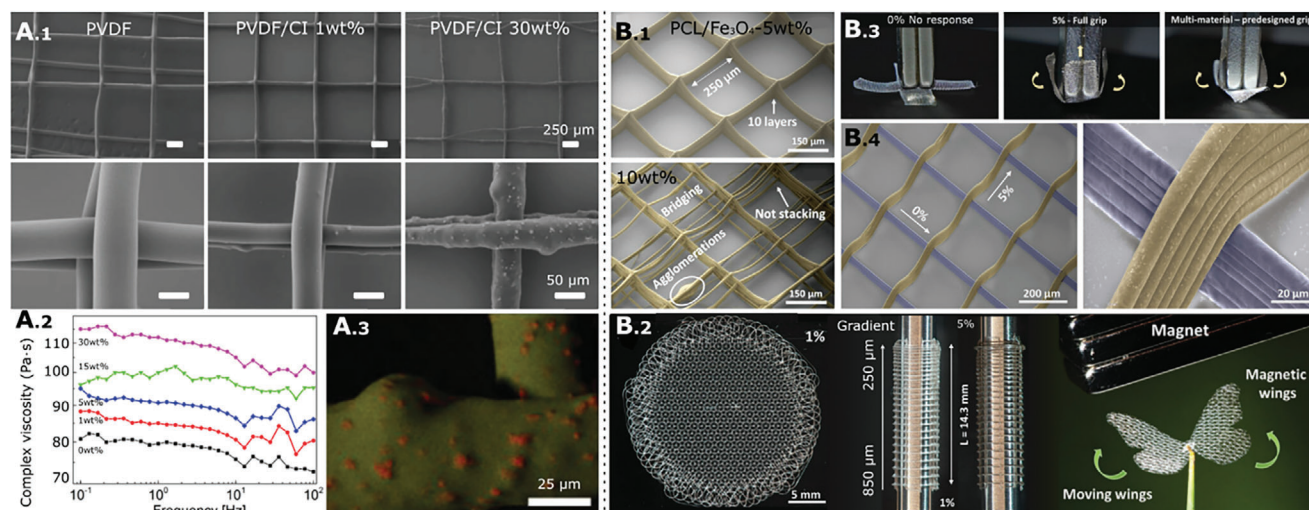


Figure 6. Detail of composite scaffolds printing with fillers that provide the samples with magnetic response: A) Carbonyl iron (CI) particles addition to PVDF scaffolds: A.1) SEM images of the neat PVDF and composites with increasing CI content. A.2) Dependence of the complex viscosity as a function of frequency for samples containing different amounts of CI (0–30 wt%) at 200 °C. A.3) EDX image of a scaffold with 30 wt% of CI particles showing homogenous distribution throughout the printed fibers (Fluorine within the PVDF is in yellow, and iron in red). B) Fe₃O₄ nanoparticles addition to PCL scaffolds: B.1) False-colored SEM images detailing the primary differences observed between the PCL/Fe₃O₄ scaffolds with 5 and 10 wt% of NPs. B.2) Photographs of hexagonal MEW microstructure with 0°/30°/60°/90°/120°/150° laydown patterns (1 wt%), tubes with gradient features and 0, 1, and 5 wt% of Fe₃O₄, and laser-cut butterfly-shaped samples for the 5 wt% filler content sample. B.3) Photographs of cross-shaped samples deflected under an external magnetic field. B.4) False-colored SEM images of the fiber intersections in the multimaterial sample. A) Reproduced with permission.^[98] Copyright 2022, Wiley-VCH. B) Reproduced with permission.^[100] Copyright 2023, Wiley-VCH.

Overall, it is demonstrated that the incorporation of fillers into the polymeric matrix for MEW printing allows the improvement of samples properties (such mechanical properties or bioactivity), and the introduction of new functionalities (such imaging capacities or magnetic response), expanding the potential of MEW across new fields. However, future research should address challenges related to high filler concentrations, homogeneous mixing of materials in blends, or the use of conductive additives to continue expanding MEW's capabilities.

4.2. Postprinting Processing

Another common approach to enhance MEW structures performance is their postprinting processing. This approach enables the modification of MEW printed structures properties beyond the limitations that fillers processing carries.^[102] The most common post-processing techniques in MEW are wet and dry etching, and coatings, including sputtering and dip coating (Figure 7). Other alternatives are chemical functionalization, encapsulation, and annealing, which are less explored for MEW, but highly interesting for expanding MEW structures functionality. Most of the currently explored MEW postprocessing approaches are directed to improve printed structures bioactive response, especially with PCL.^[40] However, other modifications that expand the MEW multifunctionality have been also explored. A detailed analysis of the reported MEW structures postprocessing is given in the following and summarized in Table 3.

PCL is inherently hydrophobic and lacks bioactive cues, which has prompted researchers to explore different approaches to address these limitations. A commonly explored approach are

etching treatments, consisting on selectively remove material from the materials surface and introduce new chemical functional groups or active sites.^[103] In MEW, wet etching, usually consisting of PCL immersion in an alkaline bath, is broadly employed to increase PCL fiber hydrophilicity. One example is the work by Muerza–Cascante and co-workers, in which they treated the MEW scaffolds in a NaOH bath, resulting in increased fiber roughness, reduced hydrophobicity, and enhanced protein absorption and cell attachment.^[104] Meng and colleagues also applied NaOH etching to PLLA scaffolds, achieving increased hydrophilicity, surface roughness, and osteoinductive capacity (Figure 7A).^[54] Another employed method, consisting on using an active plasma to remove material from the fiber surface, is dry etching. A good example is the work of Ainsworth and colleagues, in which an atmospheric-pressure plasma jet (APPJ) treatment was employed to enhance scaffolds hydrophilicity, and then covalently attach TGFβ1 proteins to the scaffold (Figure 7B).^[105] Scaffolds containing attached TGFβ1 proteins, show a significantly increased compressive modulus (more than threefold) and increase neo-cartilage matrix production, when compared to a standard protein-in-medium approach. Despite their simplicity, etching treatments usually have a limited modification ability, and thus are commonly used as pretreatment to enhance other post-treatments efficiency.

One of the most widely explored post-treatments to fully tackle PCL limitations are coatings. In this case it is important to note that the addition of material as coating increase the fiber diameter, thus the control of coating thickness is essential to avoid large variations of scaffold dimensions. Calcium phosphate (CaP) coatings are the most explored ones to modify MEW printed PCL structures due to their potential to

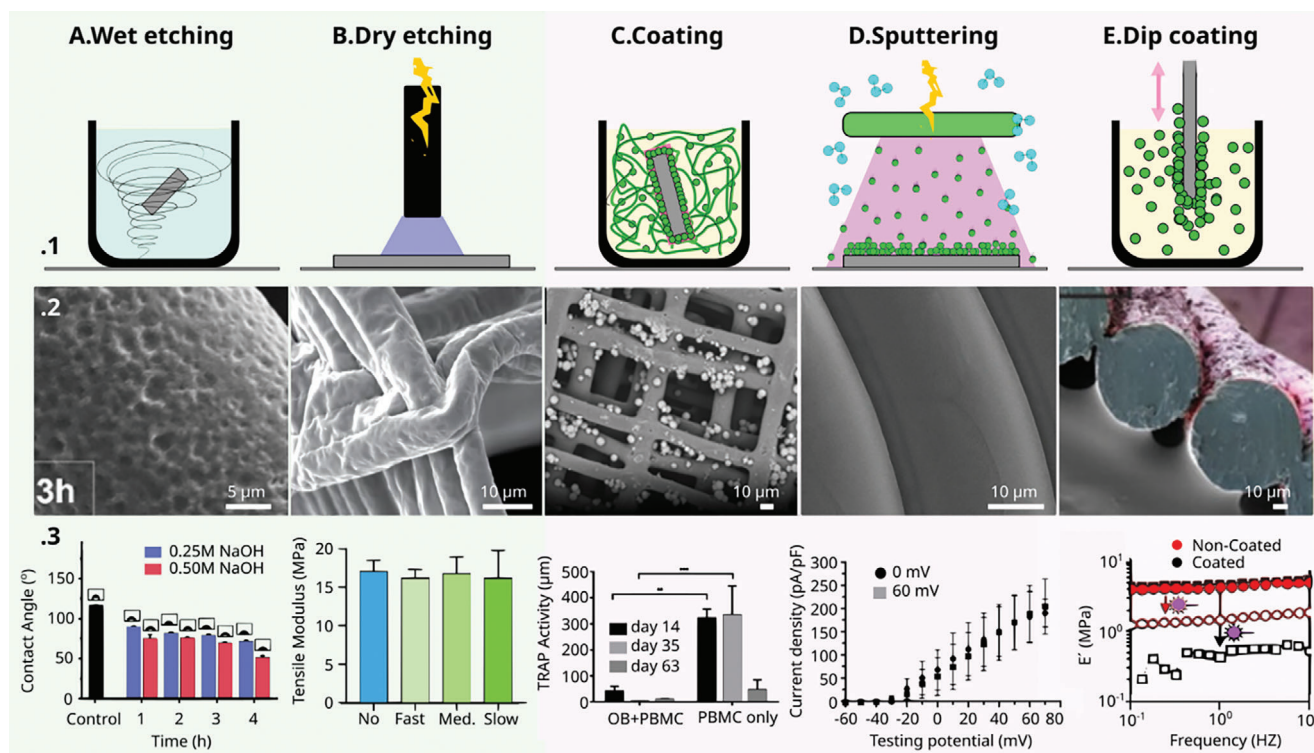


Figure 7. Main postprocessing treatments performed on MEW scaffolds: A) Wet etching. B) Dry etching. C) Coating. D) Sputtering, and E) Dip coating. A.2–E.2) Representative SEM images of postprocessed MEW scaffolds showing the modifications on the fiber surface by the methods described in A.1–E.1, respectively, and A.3–C.3) representative graphics of post-printing processing effect on MEW scaffolds: A.3) decrease on contact angle with increasing etching times. B.3) variation of tensile modulus with etching parameters. C.3) TRAP activities of cells seeded on CaP-coated PCL scaffolds. D.3) current densities of PC12 cells with and without EM stimulation, and E.3) change on storage modulus under light exposure for coated and noncoated MEW structures. A) Reproduced with permission.^[54] Copyright 2022, Elsevier. B) Reproduced with permission.^[105] Copyright 2023, Wiley-VCH. C) Reproduced with permission.^[106] Copyright 2019, MDPI. D) Reproduced with permission.^[112] Copyright 2023, Springer Nature. E) Reproduced with permission.^[75] Copyright 2023, Wiley-VCH.

reduce the PCL fiber hydrophobicity and enhance their osteo-inductive properties. One example of that is the work by Brown and colleagues, where they coated PCL tubular structures with CaP to facilitate the attachment and growth of primary human osteoblasts (hOBs) and provide a bone-mimicking crystalline microenvironment.^[81] Coated fibers exhibited increased roughness compared to noncoated fibers, potentially contributing to enhanced cell–material interactions. Similarly, Hammerl and co-workers deposited CaP particles on the PCL fiber surface (Figure 7C).^[106] Results show variations on cells behavior depending on the samples, being remarkable the formation of multinucleated giant cells for the PCL/CaP scaffolds cultured with peripheral blood mononuclear cells (PBMC), or a higher density of extracellular matrix (ECM) mineralization on functionalized scaffolds. Abbasi et al. also investigated the coating of PCL scaffolds with CaP and compared the main properties between coated and noncoated scaffolds.^[107] In this case the coating was as a homogeneous layer, with a clear increase in fiber roughness. CaP coating significantly reduced the hydrophobicity of the PCL scaffolds and greatly increased the total surface area, as demonstrated from Brunauer–Emmett–Teller (BET) analysis. Besides, improved cell proliferation, and spreading of osteoblasts was achieved. Finally, Farag and colleagues deposited a CaP bioactive layer with nanostructured morphology (nanoflakes) onto PCL

MEW scaffolds to stimulate rapid bone formation for periodontal regeneration.^[108] Coated PCL scaffolds show remarkable and progressive mineralization of the ECM laid down by human alveolar bone-derived osteoblasts (hOBs).

Driven by the improvement of MEW scaffolds osteogenic performance, Su and colleagues explored alternative PCL coatings with ZnO nanoparticles (ZnO NPs) and nanoflakes (ZnO NFs).^[109] Those coatings, confer piezoelectric properties to the MEW scaffolds, which also exhibited increased calcium mineralization levels. In particular, calcium mineralization levels of MC3T3 osteoblasts cultured on the ZnO NPs functionalized scaffolds were found to be ≈ 3.91 -fold higher than those cultured on nonfunctionalized PCL scaffolds. Further, the scaffolds functionalized with ZnO NFs show an ≈ 2.17 times higher mineralization compared to PCL/ZnO NPs structures, due to their biomimetic topography.

Also with the aim of improving the bioactivity of MEW scaffolds, Mirzaei et al. investigated PCL scaffolds functionalization with anti-inflammatory yeast-derived peptides (VLSTSF-PPW (VW-9)).^[101] Functionalized scaffolds exhibited improved fibroblast and macrophage penetration, increased cell proliferation and superior anti-inflammatory properties. An alternative strategy to improve cells infiltration onto MEW scaffolds was proposed by Ryma et al. which leveraged the phase separation

Table 3. Main postfabrication functionalization processes applied to MEW scaffolds to improve their properties or introduce new functionalities.

Polymer	Processing	Purpose/effect	Refs., Year
PCL	CaP coating (800 nm thick)	Enhance osteo-induction.	[81], 2012
	CaP particles coating	Allow formation of multinucleated giant cells.	[106], 2019
	Nanotextured CaP coating	Significant reduction on the hydrophobicity of the scaffold. Increase in fiber roughness.	[107], 2019
	CaP coating ($\approx 310 \pm 46$ nm) with nanostructure morphology (nanoflakes-like)	Bioactive layer improve the osteo-inductive capability.	[108], 2023
PCL	NaOH etching	Enhance hydrophilicity, protein absorption and cell attachment.	[104], 2017
PLLA	NaOH etching	Enhance hydrophilicity and surface roughness. Promote higher osteo-inductive ability.	[54], 2022
PCL	Atmospheric-pressure plasma jet (APPJ) functionalization + TGF β 1 biomolecule immobilization	APPJ treatment enhances hydrophilicity and increases TGF β 1 loading efficiency. TGF biofunctionalized scaffolds stimulate neo-cartilage matrix production.	[105], 2023
	Coating with piezoelectric ZnO nanoparticles and nanoflakes	Enhance osteogenic differentiation with a larger amount of calcium mineralization compared with noncoated structures. Nanoflakes show superior osteogenic performance than nanoparticles.	[109], 2022
	Peptides grafted using EDC/NHS carbodiimide chemistry and thiol chemistry	Improvement on fibroblast and macrophage penetration and adhesion. Increased cell proliferation and superior anti-inflammatory properties.	[101], 2023
PCL/PVAc	Ethanol dissolution of PVAc	Structurally collagen-mimetic nanofibrillar structures (\varnothing of 0.25–1.5 μ m) that improve cell infiltration.	[24], 2021
PnPrOx/	Water dissolution of PcyeloPrOx		
PcPrOx			
PCL	Vancomycin drug loading by a modified solvent evaporation technique	Antibacterial activity against <i>S. aureus</i> .	[110], 2023
	NCO-poly(ethylene oxide-stat-propylene oxide) coating + streptavidin/collagen biofunctionalization	Hydrophilizes the PCL surface and minimizes unspecific interactions with proteins and cells, providing a more biocompatible interface and possibilities for further biofunctionalizations.	[111], 2019
	PPy functionalization by in situ chemical oxidative polymerization of Ppy	Confers electroconductive properties close to those reported of human myocardium while maintaining cytocompatibility with human MSCs.	[113], 2020
	Gold coating via sputtering (50 nm)	Electrical stimulation regulate cardiomyocyte contraction	[114], 2022
	Gold coating via sputtering (10–80 nm)	Provide conductivity and promote neurite outgrowth and neural cell differentiation. Gold layer also improve the mechanical performance.	[115], 2020
	Titanium (4 nm) + gold (80 nm) coating by GLAD	Wireless electromagnetic neural stimulation patches with increased neurite outgrowth.	[112], 2023
	Ti ₃ C ₂ T _x MXene coating	MXene coating allow guided neuronal growth and photothermal stimulation.	[116], 2023
	Iron oxide nanoparticles coating	Functionalized samples show potentials for magnetic hyperthermia-treatments. Higher cell adhesion and proliferation are also achieved.	[117], 2023
PETOzi	Surface functionalization with fluorophores and peptides	Surface functionalization facilitates visualization and cell attachment.	[65], 2019
TPU	Deposition of a light-to-heat converting ink layer (0.9 ± 0.1 μ m) by dip coating	The coating provides light-sensitive switchable topographies as a result of the temperature increase upon illumination.	[75], 2023
PBA-75			

of PCL/PVAc and PnPrOx/PcyeloPrOx mixtures, to produce microfibrillar bunches by dissolving one of the phases.^[24] On a different approach, Mathew and colleagues explored the use of modified solvent evaporation techniques to load MEW PCL scaffold with vancomycin drug.^[110] A high encapsulation efficiency over 89% was achieved by this method. PCL scaffolds loaded with different amounts of vancomycin (5, 10, and 25 wt%) showed high antibacterial activity against *S. aureus* even after 14 days of continuous release of vancomycin in PBS at 37 °C. Interestingly, the hydrophilic nature of vancomycin also facilitated cell attachment and proliferation, while not adversely affected mechanical or biological properties, further supporting samples potential for tissue engineering applications.

With the aim of designing a more biocompatible surface for MEW scaffolds, Bertlein and colleagues investigated multistep postprocessing to achieve permanent hydrophilization and bioactivation of PCL scaffolds.^[111] First they used an alkaline pretreatment to improve following steps efficiency, and then added a NCO-poly(ethylene oxide-stat-propylene oxide) (sp(EO-stat-PO)) hydrogel layer. The coating provides a protein-repellent and thereby more biocompatible interface due to increased surface hydrophilicity. Alternatively, they achieved a generic immobilization of biomolecules (streptavidin and collagen) into the scaffolds by linking diazirine-bearing photoleucine into the coatings.

To provide MEW scaffolds with new properties, various post-processing approaches have been also explored. For instance,

Olvera and colleagues developed electroconductive cardiac patches by coating PCL scaffolds with polypyrrole (PPy) through in situ chemical oxidative polymerization of pyrrole (Py).^[113] This endowed the MEW scaffolds with electroconductive properties ($2.73 \pm 0.3 \text{ S m}^{-1}$) suitable for cardiac patches tissue engineering ($2.4\text{--}13.6 \text{ S m}^{-1}$) while maintaining cytocompatibility with human MSCs. In a similar approach, Wang et al. investigated PCL scaffolds coated with gold as cardiac patches to regulate cardiac contraction.^[114] In this case, anisotropic sinusoidal structures were designed to mimic the collagen fiber architecture in the heart and sputtering was employed to deposit 50 nm gold layers, achieving anisotropic electrical properties in the range of $0.7\text{--}1.1 \text{ S m}^{-1}$. Electrical stimulation of the patches induced frequency-mediated synchronous contractions of HL-1 cardiac cells, while only random cells oscillations were observed without electrical stimulation. This electrical synchronization is a very interesting approach to provide reinforcement of the injured tissue and prevent arrhythmia. Similar gold coated structures were further investigated for neural stimulation applications by the same group.^[115] In this case, gold layers of different thickness were deposited on the fibers' surface, resulting in increasing electrical conductivities from 0.12 to 1.39 S cm^{-1} as the Au layer thickness increased from 10 to 80 nm, respectively. Gold-coated scaffolds were tested for their ability to stimulate PC12 electrically excitable cells, demonstrating increased cell proliferation and neurite growth with thicker gold coatings, indicating the positive effect of gold coating for cell differentiation. These gold-coated scaffolds also exhibited superior mechanical performance and flexibility, making them suitable for injection and repeated use. Giving a step forward, this group explored a wireless electromagnetic (EM) stimulation system as an alternative to wired one, which enhances the convenience of electrical stimulation and extends the applicability of these devices.^[112] In this case, the possibilities of wireless EM stimulation was investigated, together with the effect of the patch microstructural design for promoting neurite outgrowth of PC12 cells (Figure 7D). Significant increases in neurite outgrowth upon wireless EM stimulation was achieved compared to previous works on nonwireless stimulation. Furthermore, an increase in neurite outgrowth when employing straight patches instead of circular was also observed, demonstrating the importance of the microstructural design control provided by MEW. More recently, Li and colleagues explored the coating of PCL MEW scaffolds with $\text{Ti}_3\text{C}_2\text{T}_x$ MXene for a similar purpose.^[116] This MXene coating increased the hydrophilicity, cell adhesion, and electrical conductivity of the PCL scaffold. More importantly, this functionalization provides the samples with guided neuronal growth and photothermal stimulation capabilities, achieved by inducing local temperature increases in the scaffold upon red light illumination, which is highly interesting in this field. Interestingly, it should be noted that all these works are focused on providing a more active response (electroactive) and hence provide new insights to extend the possibilities for MEW structures applicability in other fields such as electronics. Driven by introducing magnetic properties in the MEW scaffolds, Unalan and colleagues explored recently the functionalization of PCL scaffolds with superparamagnetic iron oxide nanoparticles (SPIONs) and silica-coated-SPIONs.^[117] Modification of MEW scaffolds using alkaline surface treatment was previously performed to improve the coating process with the SPIONs. Cytocompatibility as-

says showed a nontoxic effect and enhanced cellular activity of MG-63 osteoblast-like cells for the functionalized scaffolds. More important, functionalized samples showed the ability to generate heat, useful for hyperthermia-treatments, when subjected to an alternating magnetic field. Finally, in a more multiactive focus approach, Constante and colleagues explored the dip coating of a shape memory TPU MEW structure with a light-to-heat converting ink ($0.9 \pm 0.1 \mu\text{m}$) (Figure 7E).^[75] This coating provides the samples with light-sensitive switchable topographies, making hard fiber stacks become soft upon illumination, and hence deformable, due to their temperature increase near their melting temperature. This structure was finally employed to create smart light-controlled valves with potential applications in microfluidics devices for controlled fluid mixing.

Overall, postprinting treatment have demonstrated to play an essential role in enhancing the properties and functionalities of MEW structures, expanding the possibilities for utilizing MEW structures in diverse fields. Thus, proper consideration of post-processing techniques is also key when exploring new applications for MEW.

4.3. Combination with Other Techniques

Another promising strategy to fully harness the potential of MEW is to combine this technique with others in a multitechnique fabrication approach, creating hybrid designs with improved properties by leveraging the specific advantages of each procedure, while increasing design freedom. Some of these approaches are based on novel processing technologies, combining multiple techniques in a single device that either work at the same time or have switchable modules while others are based on a layer by layer or multistep fabrication process, as reported on the following and summarize on Table 4.

One of the earlier applications combining MEW with other techniques focused on microfluidic devices development. By leveraging deposition accuracy, fiber homogeneity, and featured dimension provided by MEW, the MEW processed fibers are employed as sacrificial phase to define microfluidic channels. Subsequently, a second material is used to encapsulate MEW processed fibers and generate the permanent part of the microfluidic device. Finally, the MEW fibers are either peeled off or dissolved to create microchannels within the permanent component. By tuning the MEW processing parameters and design, channels shape and dimensions can be finely tuned. One such example is the embedding of PCL MEW scaffolds within poly(2-alkyl/aryl-2-oxazoline) (PAOx) hydrogel, followed by dissolving the PCL structure with an acetone-water mixture to produce hydrogels with well-defined 3D porous channels.^[118] In a similar approach, PCL scaffolds were embedded within poly(ethylene glycol) (PEG) hydrogels by direct casting to later define hollow channels within the hydrogel after removing the PCL by either dissolution with acetone or by manual extraction.^[119] In this work, not only MEW fibers but also FFF printed parts were employed to define channels with different sizes, ranging from 50 to 500 μm . Besides, a selective patterning of the hollow channels surface with peptides was performed, which allowed to support cells growth and guide on the channels. Focus also on cell culture systems, Liu and co-workers patterned PCL fibers via MEW inside different

Table 4. Hybrid structures developed by combining MEW with other fabrication techniques.

	Structure	Application	Refs.	
MEW (sacrificial) + encapsulation	PAOx hydrogel + acetone-water mix to dissolve the MEW PCL	Approach to create well-defined multilevel control over interconnected pores with diameters in the lower micrometer range inside hydrogels	[118], 2016	
	PEG hydrogel + manual MEW PCL removal or by acetone dissolution	Peptide-decorated hydrogel channels to enable precise spatial peptide patterning for cell guidance.	[119], 2020	
	Hydrogel (GelMA, HAMA, alginate and agarose) + MEW PCL removed by pulling	Interconnected, perfusable microchannels within cell-laden hydrogels, matching capillary density in human tissue, promising applications in tissue models and microfluidics.	[120], 2023	
	PDMS mold + MEW PCL peeling	Versatile microfluidic device manufacturing.	[121], 2018	
	PDMS mold + MEW fiber dissolution in water		[66], 2021	
	GelMA hydrogel + MEW scaffold dissolved on PBS solution	Facile and flexible approach for the integration of biomimetically branched microvasculature within bulk hydrogels.	[122], 2022	
MEW + hydrogel	MEW + GelMA and alginate hydrogels	Hydrogel reinforcement with highly organized MEW microfiber networks. Tunable composites stiffness and elasticity increase respect to hydrogel or MEW scaffolds alone (up to 50-fold).	[123], 2014	
	MEW + GelMA/HAMA hydrogel		[124], 2015	
	MEW + sPEG/Hep hydrogel		[125], 2017	
	MEW + Photocrosslinkable gelatin		[86], 2022	
	MEW + Gelatin/genipin/bioglass hydrogel		[55], 2022	
	MEW + ELR hydrogel	MEW provide a macroporous structure, while the microporous structure is provided by the hydrogel, favoring adequate cellular infiltration.	[126], 2022	
MEW + hydrogel (CHTMA, GELMA, LAMMA, and HAMA)		Thermoresponsive MEW fibers provide hydrogel composites with shape memory ability.	[76], 2022	
	MEW + Solution electrospinning	SES membrane + MEW ordered fibers on top	SES support the formation of a confluent endothelium while the outer MEW layer allow a fast cell colonization.	[127], 2019
		PCL MEW lattice + drug-loaded PCL SES mat	MEW structure increases the strength of the drug-delivery SES membrane and the elongation to break. Solvent vapor annealing is applied to adjust the drug release of the SES membrane.	[128], 2022
		PCL MEW lattice +	MEW structure confers the hybrid membrane with a hydrophobic character, while the PAN-SiO ₂ electrospun mat is hydrophilic which generates an asymmetric wettability that allows for directional water transport.	[129], 2022
		PAN-SiO ₂ SES mat		
		PCL gradient porous structure by MEW + PAN-SiO ₂ SES mat		[130], 2023
MEW + extrusion printing		Cells loaded GelMA hydrogel + PCL fibers	Fabrication of mechanically stable constructs with precise spatial distributions of different cell types.	[131], 2019
	GelMA with collagen/Matrigel bioinks + PCL MEW scaffolds	A patterned prevascularized myocardial construct fabrication. MEW fiber reinforced the hydrogel while maintaining control over cellular composition, type, and density.	[132], 2023	
	AA-MA + PCL fibers	Tubular scroll-like bilayer scaffold with excellent viability and proliferation. MEW fibers allow a high degree of cells orientation.	[133], 2021	
	HA-MA + PCL-PU fibers	Shape-changing bilayered scaffolds for the growth of muscle cells with preferential alignment provided by the MEW fibers.	[51], 2021	
	CPC fibers (300 μm) + PCL microfibers (28 μm)	MEW improves integrity while not affecting mechanical stiffness. PCL microfibers also allow a bridging effect of hMSC cells through CPC big pores by acting as support.	[134], 2022	
	MEW + fused filament fabrication	PCL tick FFF fibers (300 μm) + MEW microfibers (20 μm)	Auxetic scaffolds designed to tune the Poisson's ratio based on the intended deformation mechanism or tissue environment. MEW fills the pore for promoting the cell growth by offering structural support.	[135], 2022
PCL tick FFF fibers (250 μm) + MEW microfibers (20 μm)		Open-source low-cost filament based MEW devices modified from a commercial Voron FFF printer allow to combine FFF and MEW with a single nozzle and all at once.	[32], 2023	
PDO tick FFF struts (430 μm) + MEW microfibers (30 μm)		Common Prusa FFF printer modified to integrate MEW and combine FFF and MEW for dual-mode fabrication. Allow for different cell growth behaviors.	[13], 2023	

(Continued)

Table 4. (Continued)

	Structure	Application	Refs.
MEW + inkjet printing	PCL MEW scaffolds + MSCs cells loaded by inkjet on the pores	Inkjet printing to deposit specific cells into MEW pores. MEW allows to orient the growth of generated cellular aggregates, and provide tensile reinforcement.	[136], 2022
	PCL MEW scaffolds + MSCs cells-alginate bioink loaded on the MEW pores	Fibrocililage grafts with user defined collagen architectures and anisotropic mechanical properties. MEW structure influences the spatial organization of the collagen network laid down by the jetted cells.	[138], 2023
MEW + volumetric printing	Tubes of PCL by MEW + GelMA	Tensile, burst, and bending mechanical properties of printed tubes are improved and tuned by altering the MEW structure design resulting in tubular constructs which better mimic native tubular tissues of biological relevance, such as vascular structures.	[137], 2023

hydrogels (GelMA, HAMA, alginate, and agarose), and then pulled out the fibers, giving rise to capillary-scale channels within the hydrogels, offering an alternative fabrication technique toward microfluidic delivery of nutrients within 3D cell culture systems (Figure 8A).^[120] From a different fabrication perspective, Zeng and colleagues explored the design of microfluidic channels inside PDMS structures by first casting the PDMS on PCL MEW patterns, then peeling the patterned PDMS from the sacri-

ficial MEW layer, and finally bonding the PDMS with the defined microchannels to another PDMS layer by hot pressing.^[121] In order to illustrate the applicability of this approach for microfluidic devices fabrication, T-shape and cross-shape channel structures were designed and employed to respectively create laminar flow and microdroplets. Recently, Ryma et al. explored other materials for define the MEW sacrificial templates, highlighting the use of Isomalt sugar to fabricate channels within PDMS molds

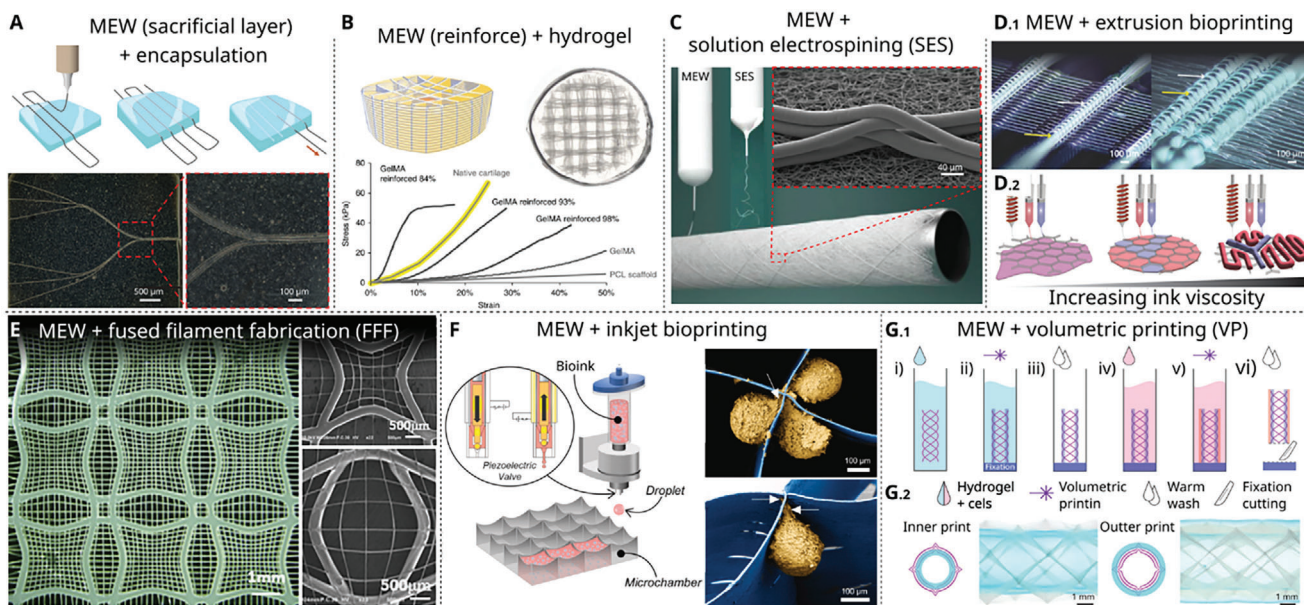


Figure 8. Hybrid structures fabricated by combining MEW and other techniques: A) Creation of channels within hydrogels by casting MEW fibers in the hydrogel, together with images of the obtained microfluidic channels. B) Schematic and optical image of PCL scaffolds as a reinforcing component on GelMA hydrogel, together with stress–strain curves comparing mechanical properties of MEW scaffold, hydrogel, and their combinations. C) Preparation scheme and SEM image of bilayer tubular scaffolds consisting on a nonwoven solution electrospinning inner layer and MEW oriented fibers on top. D. 1) MEW fibers guided over an extruded hydrogel (Pluronic, 40% w/v). D. 2) Representation of extrusion printing into MEW meshes with expected outcomes based on polymeric/cross-linked density of hydrogel. E) Demonstration of the multiscale scaffolds combining FFF struts with MEW microfibers. F) Biofabrication process of inkjet printed bioinks into a box-like MEW structure, together with SEM images of self-assembled spheroids in MEW scaffolds 48 h after inkjet printing. G) MEW combination with VP: G. 1) Sequential VP printing of cell-laden, multimaterial, and multilayer tubular constructs, and G. 2) Graphical overview of possible inner and outer printing strategies, in which the hydrogel embeds only the inner or outer region of the MEW construct. A) Reproduced with permission.^[120] Copyright 2023, Wiley-VCH. B) Reproduced with permission.^[123] Copyright 2015, Springer Nature. C) Reproduced with permission.^[127] Copyright 2019, Wiley-VCH. D. 1) Reproduced with permission.^[131] Copyright 2019, Wiley-VCH. D. 2) Reproduced with permission.^[132] Copyright 2023, IOP Publishing. E) Reproduced with permission.^[135] Copyright 2021, Elsevier. F) Reproduced with permission.^[136] Copyright 2022, Elsevier. G) Reproduced with permission.^[137] Copyright 2023, Wiley-VCH.

after a water-based dissolution of the Isomalt MEW fibers,^[66] or the encapsulation of PycloPrOx MEW fibers on GelMA hydrogels and their subsequent dissolution on a PBS solution to create perfusable and functional microvascular networks within bulk hydrogels.^[122] Overall, these works demonstrate the potential of MEW as a sacrificial technique for fabricating microfluidic devices with well-defined microstructures.

MEW scaffolds have also been commonly embedded between hydrogels as reinforcement. This strategy mimics biological tissue organization, in which natural fibers reinforce soft matrix tissues, and allows to adjust the mechanical properties of soft hydrogels to match specific tissues behavior. Different examples of that can be found in the literature while just some of the most relevant and recent ones are highlighted in the following. For instance, Visser and colleagues reinforced GelMA and alginate hydrogels with PCL MEW scaffolds.^[123] It was found that the stiffness of the hydrogel/scaffold composites significantly increased up to 54-fold, compared with hydrogels or microfiber scaffolds alone, approaching mechanical behavior of some tissues (Figure 8B). These structures show the capacity to support cell proliferation and extracellular matrix production in a diversified environment. Besides, they gather advantages related to materials degradation rates, since the hydrogel is degraded in some days, while PCL degrades in years. This allows tissue regeneration while maintaining a temporary reinforcing network. In a similar approach, Bas et al. reinforced GelMA and GelMA/HAMA hydrogels with PCL MEW fibers.^[124] This resulted in improved compressive properties, with more than a 35-fold-increase of the compressive Young's modulus and a decrease on the Poisson's ratio. In this case, the effect of scaffold structure on the reinforcement properties was also explored, showing that the reinforcement is also affected by the defined microstructure. Later on, this group explored the reinforcement of a poly(ethylene glycol)/heparin (sPEG/Hep) hydrogel with PCL MEW scaffolds, to create viscoelastic, mechanically nonlinear, and anisotropic composites.^[125] Further, composites exhibited enhanced biological performance, providing a suitable microenvironment for in vitro human chondrocyte culture and neocartilage formation. More recently, Afghah et al. explored the application of PCL MEW scaffolds filled with a photocrosslinkable gelatin hydrogel loaded with growth factors for wound healing.^[86] Further, the addition of bioactive glass within the composite to further improve the wound healing was investigated. Fabricated composites exhibited a huge increase on the tensile modulus while maintaining cell viability and cytocompatibility, which is further improved by the bioactive glass presence, making them suitable for skin tissue engineering. Similarly, Meng and colleagues explored a gelatin/bioglass hydrogel but with PLLA structures as the MEW reinforcement matrix, achieving enhanced mechanical and biological performance.^[55] Different bioglass concentrations from 0 to 10 wt% were investigated showing that the best performance was achieved for the samples with 1 wt%, which show higher storage modulus and superior in vitro osteoinduction capability.

Other common approach combining MEW scaffolds and hydrogels is to employ the hydrogel for filling the macropores of MEW constructs to improve the biological response. One example is the work by Saily and colleagues in which they embedded a PCL macroporous MEW structure with a microporous elastin-like recombinamer (ELR) hydrogel to develop a

soft-network composite providing both the structural integrity required to withstand the demanding cardiovascular loading conditions and adequate porosity to enable fast and adequate cellular infiltration.^[126] Finally, driven by a more active focus approach, Costa and colleagues investigated the combination of thermoresponsive SMPU MEW scaffolds embedded within different hydrogel networks (GELMA, CHTMA, LAMMA, and HAMA) to provide them with shape memory ability.^[76] By using this approach, hydrogels show shape fixity ratios from 50% to 90% and excellent shape recovery ratios ($\approx 100\%$) at body temperature (37 °C). Cytocompatibility tests further demonstrated good viability of the composites, which open plenty of possibilities for using these structures for tissue engineering and regenerative medicine.

Another frequently explored approach is to combine MEW with solution electrospinning (SES). Given the similarities between both techniques in terms of operation, driven by applied electric fields, the combination of both techniques is not complex, and can even be carried out in a single device. One example is the work by Jungst and colleagues, where they developed a PCL hybrid tubular structure combining MEW and SES to mimic the structure of native blood vessels.^[127] This bilayer structure comprised an inner layer of randomly oriented dense SES fiber mesh and an outer layer of MEW microfibers with controlled orientation (Figure 8C). The SES layer supported endothelium formation on the inner surface while the MEW layer facilitated a fast vSM-like cells colonization in a 3D-oriented manner. With different aims, Xu and colleagues also developed a bilayer SES-MEW planar structure.^[128] In this case, the MEW layer enhances the mechanical properties of the nonwoven fabric, increasing the elongation to break from $\approx 170\%$ to $\approx 900\%$ for the composite structure. The SES layer was loaded with an anticancer drug for controlled drug release. Interestingly, these authors employed a home-made multihead device to combine SES and MEW in the same device, allowing for reducing the fabrication times and increasing the design freedom. Beyond biomedicine, Du and colleagues developed a bilayer MEW-SES structure with asymmetric wettability for directional water transport.^[129] In this case, a PCL MEW structure was employed as a hydrophobic layer while a PAN-SiO₂ SES layer served as the hydrophilic layer. The pore size of the MEW layer was found to significantly affect directional water transport, with membranes having smaller MEW pores showing much lower wettability and excellent one-way water transport indexes of around 1000%. In this case, MEW and SES were carried out in the same custom device with switchable MEW and SES modules. In a similar approach, this group fabricated MEW structures with a gradual porosity, printed below and above the CTS, which further allow to tune the asymmetric wettability of the MEW-SES structures.^[130] Results showed a large increase in water one-way transport index (1281% for a fiber spacing of 300 μm). These structures have great possibilities in the field of functional textiles able to transport water rapidly from the skin to the outer and prevent the skin from being rewetted in the reverse direction. Overall, MEW and SES combination demonstrate the importance of combining MEW with other techniques to provide the printed structures with extra functionalities.

MEW has been also combined with extrusion printing, particularly in the field of bioprinting, to reinforce structures mechanically and improve their bioactivity. For instance, Ruijter

and colleagues combined extrusion-based bioprinting of cell-encapsulated hydrogels with MEW of PCL microfibers in a single-step fabrication process (Figure 8D.1).^[131] This resulted in mechanically reinforced composites, with an increase on the compressive modulus from ≈ 20 kPa for gel alone to ≈ 247 kPa for composite structures. More importantly, this setup allows for controlled distribution of different cell types along the composite structure while not compromising cell viability. Similarly, Ainsworth and colleagues explored the combination of extrusion based bioprinting of GelMA hydrogel with MEW of PCL fibers to fabricate myocardial constructs with precisely patterned prevascular pathways.^[132] In this case, different GelMA based bioinks containing collagen, Matrigel or fibrinogen and optimized for vascular and myocardial tissue formation were tested. The controlled deposition of these bioinks above a MEW mesh was demonstrated, showing a clear formation of an interface between the vascular region and the myocardium tissue after some days, indicating the possibility for endothelial cells to migrate and vascularize (Figure 8D.2).

Combining hydrogel extrusion and MEW from a more active focus approach, Constante et al. developed shape-morphing structures with potentials for cells alignment by combining PCL MEW fibers with extruded alginate.^[133] This combination allows the design of structures that undergo shape transformations, from planar to a tubular-like folded scaffold, with an anisotropic inner topography. Besides, the transformation was reversible and tunable by factors such as the environment media, the concentration of calcium ions and the structure of the scaffold. This innovative approach holds immense promise, particularly in the realm of 4D printing, where structures evolve and adapt over time in response to external stimuli. Expanding upon this concept and using a similar approach, this group developed a shape-changing bilayer structure composed of a HA-MA extruded hydrogel and PCL-PU MEW fibers.^[51] The fabricated structures exhibited a remarkable ability to respond to external stimuli by either rolling up or reverting to their original form, all while facilitating cell proliferation and alignment within the folded structures. Interestingly, the shape-changing response in this case is not provided by the extruded HA-MA but rather by the PCL-PU MEW fibers with inherent shape-morphing properties. This noteworthy discovery underscores the versatility of both techniques in conferring shape transformation capabilities to composite materials, provided the materials are chosen properly.

Finally, Kilian and co-workers explored the fabrication of a multilayered structure combining extrusion-based 3D printing of calcium phosphate cements (CPC) and MEW of PCL fibers with the aim of reducing the inherent brittleness of CPC.^[134] The introduction of PCL fibers holds the CPC fragments in place, hence enhancing the robustness of the CPC scaffolds that alone lose their structural integrity entirely upon fracture. Furthermore, the seeding efficiency of various structures was also investigated, revealing that the incorporation of PCL MEW fibers played a pivotal role in bolstering seeding efficiency and facilitating pore bridging effects above a certain critical CPC strand distance.

Focused also on mechanical reinforcement and cell adhesion improvement, different authors have combined MEW with FFF. Both MEW and FFF operate with heated polymers in an

extrusion-based mode, with the primary distinction lying in the applied voltage for MEW and the polymer feeding methods—continuous filament extrusion versus heated syringe reservoir, respectively. These similarities facilitate the combination of both techniques in a single device. In fact, recent years have witnessed the emergence of instruments capable of seamlessly integrating both techniques. An example of that is the work by Jin and colleagues, in which they repurposed a MEW device to function as direct ink writing (DIW) system by deactivating the voltage component and significantly increasing the applied pressure and reducing the nozzle-to-collector distance similar to FFF operation mode.^[135] They successfully engineered tunable auxetic PCL patterns with thick fibers to finely adjust the Poisson's ratio and used MEW fibers to fill these auxetic structures to foster cell growth (Figure 8E). More recently, different groups have harnessed the potential to transform FFF devices into MEW systems by introducing a high voltage supply. This innovative approach mitigates common MEW material degradation issues, thanks to reduced heating times in filament-driven systems, while also unlocks the ability to seamlessly integrate both thick and thin fibers by just reconfiguring the printing setup. One example of that is the work by Reizabal and colleagues who employed the open-source MEWron system to combine both thick and thin PCL fibers within a single structure through simple adjustments in the nozzle-to-collector distance and applied voltage.^[32] Another noteworthy demonstration is the work by Mueller and colleagues in which they transformed a commercial Prusa FFF printer into a MEW device and demonstrated the possibilities of both techniques combination by developing PDO multilayer structures.^[13]

More recently, the integration of MEW with other advanced techniques, such as inkjet bioprinting and volumetric printing, has opened up exciting possibilities in the realm of tissue engineering. A notable example is the work by Dufour and colleagues who utilized MEW to create square arrays of PCL structures, subsequently filling them with cell suspensions via inkjet bioprinting (Figure 8F).^[136] In this approach, MEW arrays served a dual purpose: directing the growth of cellular aggregates within the structures in a well-distributed and reproducible manner, while also bolstering the hybrid construct's tensile strength and stiffness. In a similar approach, the same group explored the application of these structures to engineer fibrocartilage grafts with user defined collagen architectures.^[138] In this endeavor, they designed MEW and FFF structures with varying pore architectures and fiber diameters, subsequently loading them with cell-laden bioink through inkjet bioprinting. It was found that the different microchamber architectures fostered distinct cartilage phenotypes and enabled the preferential direction of collagen deposition by modifying the pore architecture. Interesting, the compressive stiffness of structures generated using FFF far exceeded that of native meniscus tissue, whereas those generated by MEW closely 'mated' the mechanical properties of native tissue, offering the potential to develop fibrocartilaginous tissues with compressive mechanical properties similar to those of native meniscus.

Finally, Größbacher and colleagues explored the combination of MEW with volumetric printing (VP).^[137] In this case, tubular PCL MEW structures were first fabricated and subsequently introduced into a VP vial along with a GelMA bioresin and exposed

to the tomographic light projections necessary for the formation of 3D objects via VP (Figure 8G). VP inherently results in structures with limited mechanical stability due to the use of soft material. Hybrid MEW-VP fabrication approach emerged as a compelling solution to enhance mechanical properties while preserving the design intricacies offered by VP for hydrogels. Tensile and bending mechanical properties of printed tubes were successfully fine-tuned by modifying the MEW design and adjusting the number of layers. As a result, the hybrid constructs closely approached the mechanical characteristics of native tubular tissues with biological relevance. Furthermore, this approach showcased the potential to create hierarchical living constructs by replicating the three distinct layers found in native macrovessels, exemplifying the potential of the MEW-VP approach.

Overall, combining MEW with other fabrication techniques has proven to be a powerful strategy for enhancing the properties of other materials, as well as the reach of other techniques. These hybrid approaches offer advantages in terms of mechanical reinforcement, controlled drug release, and tissue-specific architectures, and is an approach that is expected to continue growing in the future.

5. Conclusions and Future Trends

MEW has emerged as a potentially transformative technology in the realm of AM, offering exceptional precision and reproducibility, while enabling the fabrication of size relevant structures. Initially focused on processing PCL for biomedical applications, MEW has witnessed a recent surge in interest, expanding its capabilities. Currently, biodegradable polymers, elastomeric compounds, and shape memory blends are being successfully printed using MEW. MEW has also found applications beyond biomedicine, including microfluidics, soft robotics, and sensing technologies. Despite these significant achievements, MEW still faces some limitations that are gradually being overcome through innovative strategies, such as updated MEW printer generations, the processing of new materials, and the combination of MEW with other techniques.

Among the strategies to enhance and diversify MEW-processed materials, the incorporation of fillers deserves special attention. This approach not only fine-tunes the base properties, including mechanical characteristics and biodegradability but also introduces entirely new functionalities like antibacterial behavior, magnetic properties, and thermochromic responses. These new attributes hold great promise not only for biomedicine but also for expanding MEW into new fields. Postprinting processing strategies also play an important role in tailoring material properties, being often used to enhance biological responses. These techniques can also introduce new properties like electrical conductivity through straightforward and scalable steps. Integrating MEW with other technologies further broadens its horizons and allows for the incorporation of its high-resolution features into larger-scale systems. This integration, particularly with soft materials like hydrogels, presents promising avenues for reinforcement and life tissues mimicking, among others. Overall, combining these three strategies (fillers addition, postprinting processing, and multitechnology combination), can considerably extend MEW's reach, though there are still ob-

stacles to overcome in order to establish MEW as a mainstream tool in materials science and product development and fabrication.

One of the most grassroots effort to address MEW's challenges is to improve its hardware. MEW processing technology should provide reliable devices capable of handling a wide spectrum of materials, from high-performance polymers to inks with variable viscosities. This entails not only high-quality MEW devices but also the hackability of the system to introduce advanced features such as heated mandrels, nonplanar collectors and temperature-controlled chambers. Additionally, MEW should incorporate the latest updates from other AM technologies, such as multiple head printing and material swapping tools, to enhance productivity and enable multimaterial printing. The implementation of infinite printing tools, such as conveyor belts, can also expand the effective printing surface and boost productivity. Automatic calibration tools should be also explored to widespread MEW's usage and make it more accessible to a broader audience.

Apart from hardware enhancements, the optimization and development of standardized software capable of automatically managing MEW variables, such as applied voltage and flow rate, are necessary. This would simplify the operation of the technology and unlock advanced features like massive layer stacking and variable fiber size printing. Standardized and user-friendly G-code generation tools should be also developed to facilitate the creation of novel geometries and functions, and support research efforts.

Further, as more applications are investigated, more research will develop and formulate inks suitable for MEW. This include new polymer, blends and composites, as well as, the incorporation of additives that aid in polymers processing, such as thickeners and diluents that affect the MEW jet, or stabilizers to mitigate heating-related limitations. Strategies must also be established and standardized to incorporate and modify the intrinsic properties of MEW-processed materials.

Over the next decade, MEW has the potential to become a key tool for certain high-resolution materials processing niches. The diversification of materials empowers MEW to be tested within a wide range of fields, including tissue engineering, drug delivery systems, flexible electronics, smart textiles, and microfluidics. The continuous exploration and incorporation of new materials expand the functionalities of MEW, including biocompatibility, piezoelectricity, shape memory, magnetic responses and enhanced mechanical strength. Looking to the future, 4D printing stands as a promising direction that could allow novel applications across various fields. MEW, with its fast-actuating microfibers and a high surface to volume ratio, aligns well with some requirements of 4D printing. These include filtration, textiles, water evaporation, desalination, flexible electronics, resistive sensors, soft robotics, tissue engineering, biofabrication, and cancer research. MEW produces porous materials with high surface areas, custom structures, and variable fiber diameter and therefore can be appealing to researchers across various fields, leading to increased innovation and a broader range of applications beyond biomedicine. Given the recent advancements and growing interest in MEW, its successful use in various industries will challenge the technology, and it is poised for an exciting and dynamic future.

Acknowledgements

The financial support from the Government of the Basque Country (Grupos de Investigación, IT1756-22) was appreciated. P.G.S. thanked the University of the Basque Country (UPV/EHU) for the Margarita Salas post-doctoral grant and the open access funding. P.D. is supported by the Bradshaw and Holzapfel Research Professor in Transformational Science and Mathematics Fund. The authors also acknowledged funding by the Department of Education of the Basque Government (PIBA program, Grant No. 2022333047) and by the Spanish Ministry of Science and Innovation (Grant No. PID2022-138572OB-C42).

Conflict of Interest

The authors declare no conflict of interest.

Keywords

active materials, additive manufacturing, electrohydrodynamic printing, melt electrowriting, near-field electrospinning, review

Received: November 13, 2023
Revised: February 4, 2024
Published online: March 18, 2024

- [1] S. M. Montgomery, X. Kuang, C. D. Armstrong, H. J. Qi, *Curr. Opin. Solid State Mater. Sci.* **2020**, *24*, 100869.
- [2] T. Tom, S. P. Sreenilayam, D. Brabazon, J. P. Jose, B. Joseph, K. Madanan, S. Thomas, *Results Eng.* **2022**, *16*, 100661.
- [3] Z. Huang, G. Shao, L. Li, *Prog. Mater. Sci.* **2021**, *131*, 101020.
- [4] B. Blakey-Milner, P. Gradl, G. Snedden, M. Brooks, J. Pitot, E. Lopez, M. Leary, F. Berto, A. du Plessis, *Mater. Des.* **2021**, *209*, 110008.
- [5] X. Tian, L. Wu, D. Gu, S. Yuan, Y. Zhao, X. Li, L. Ouyang, B. Song, T. Gao, J. He, X. Lin, F. Lin, J. Zhu, D. Li, *Chin. J. Mech. Eng. Addit. Manuf. Front.* **2022**, *1*, 100014.
- [6] A. Reizabal, B. Tandon, S. Lanceros-Méndez, P. D. Dalton, *Small* **2023**, *19*, 2205255.
- [7] W. E. King, G. L. Bowlin, *Polymers* **2021**, *13*, 1097.
- [8] T. D. Brown, P. D. Dalton, D. W. Huttmacher, *Prog. Polym. Sci.* **2016**, *56*, 116.
- [9] T. D. Brown, P. D. Dalton, D. W. Huttmacher, *Adv. Mater.* **2011**, *23*, 5651.
- [10] S. Loewner, S. Heene, T. Baroth, H. Heymann, F. Cholewa, H. Blume, C. Blume, *Front. Bioeng. Biotechnol.* **2022**, *10*, 896719.
- [11] K. L. O. Neill, P. D. Dalton, *Small* **2023**, *7*, 2201589.
- [12] K. F. Eichholz, I. Gonçalves, X. Barceló, A. S. Federici, D. A. Hoey, D. J. Kelly, *Addit. Manuf.* **2022**, *58*, 102998.
- [13] K. M. A. Mueller, A. Hangleiter, S. Burkhardt, D. M. Rojas-González, C. Kwade, S. T. Pammer, S. Leonhardt, P. Mela, *Small Sci.* **2023**, *3*, 2300021.
- [14] P. Mieszczanek, S. Eggert, P. Corke, D. W. Huttmacher, *HardwareX* **2021**, *10*, e00246.
- [15] M. Lanaro, A. Luu, A. Lightbody-Gee, D. Hedger, S. K. Powell, D. W. Holmes, M. A. Woodruff, *Int. J. Adv. Manuf. Technol.* **2021**, *113*, 2539.
- [16] M. Yu, K. H. Ahn, S. J. Lee, *Mater. Des.* **2016**, *89*, 109.
- [17] P. D. Dalton, *Curr. Opin. Biomed. Eng.* **2017**, *2*, 49.
- [18] A. Hrynevich, I. Liashenko, P. D. Dalton, *Adv. Mater. Technol.* **2020**, *5*, 2000772.
- [19] A. Hrynevich, B. Elçi, J. N. Haigh, R. McMaster, A. Youssef, C. Blum, T. Blunk, G. Hochleitner, J. Groll, P. D. Dalton, *Small* **2018**, *14*, 1800232.
- [20] A. Hrynevich, P. Achenbach, T. Jungst, G. A. Brook, P. D. Dalton, *Macromol. Biosci.* **2021**, *21*, 2000439.
- [21] I. Liashenko, A. Hrynevich, P. D. Dalton, *Adv. Mater.* **2020**, *32*, 2001874.
- [22] J. C. Kade, P. F. Otto, R. Luxenhofer, P. D. Dalton, *Polym. Adv. Technol.* **2021**, *32*, 4951.
- [23] H. Haag, D. Sonnleitner, G. Lang, P. D. Dalton, *Polym. Adv. Technol.* **2022**, *33*, 1989.
- [24] M. Ryma, T. Tylek, J. Liebscher, C. Blum, R. Fernandez, C. Böhm, W. Kastenmüller, G. Gasteiger, J. Groll, *Adv. Mater.* **2021**, *33*, 2101228.
- [25] E. McColl, J. Groll, T. Jungst, P. D. Dalton, *Mater. Des.* **2018**, *155*, 46.
- [26] F. Eberle, A. K. Gruska, B. Filippi, P. Stahlhut, G. G. Wallace, P. D. Dalton, S. Beirne, *Adv. Eng. Mater.* **2022**, *24*, 2100750.
- [27] T. M. Robinson, D. W. Huttmacher, P. D. Dalton, *Adv. Funct. Mater.* **2019**, *29*, 1904664.
- [28] N. Ristovski, N. Bock, S. Liao, S. K. Powell, J. Ren, G. T. S. Kirby, K. A. Blackwood, M. A. Woodruff, *Biointerphases* **2015**, *10*, 011006.
- [29] F. M. Wunner, M. L. Wille, T. G. Noonan, O. Bas, P. D. Dalton, E. M. De-Juan-Pardo, D. W. Huttmacher, *Adv. Mater.* **2018**, *30*, 1706570.
- [30] A. B. McCosker, M. E. Snowdon, R. Lamont, M. A. Woodruff, N. C. Paxton, *Adv. Mater. Technol.* **2022**, *7*, 2200259.
- [31] K. Cao, F. Zhang, A. Zaeri, Y. Zhang, R. Zgeib, M. Calzolaio, R. C. Chang, *Mater. Des.* **2023**, *226*, 111618.
- [32] A. Reizabal, T. Kangur, P. G. Saiz, S. Menke, C. Moser, J. Brugger, P. D. Dalton, S. Luposchinsky, *Addit. Manuf.* **2023**, *71*, 103604.
- [33] M. Javadzadeh, J. del Barrio, C. Sánchez-Somolinos, *Adv. Mater.* **2023**, *35*, 2209244.
- [34] H. Haag, P. D. Dalton, V. Bloemen, *Adv. Funct. Mater.* **2022**, *32*, 2201414.
- [35] M. K. Włodarczyk-Biegun, M. Villiou, M. Koch, C. Muth, P. Wang, J. Ott, A. Del Campo, *ACS Biomater. Sci. Eng.* **2022**, *8*, 3899.
- [36] C. M. Brennan, K. F. Eichholz, D. A. Hoey, *Biomed. Mater.* **2019**, *14*, 065016.
- [37] A. Dagher, I. J. de Souza Araújo, M. Castilho, J. Malda, M. C. Bottino, *Acta Biomater.* **2023**, *156*, 88.
- [38] J. Bai, H. Wang, W. Gao, F. Liang, Z. Wang, Y. Zhou, X. Lan, X. Chen, N. Cai, W. Huang, Y. Tang, *Int. J. Pharm.* **2019**, *576*, 118941.
- [39] L. Keßler, Z. Mirzaei, J. C. Kade, R. Luxenhofer, *ACS Appl. Polym. Mater.* **2023**, *5*, 913.
- [40] B. L. Devlin, M. C. Allenby, J. Ren, E. Pickering, T. J. Klein, N. C. Paxton, M. A. Woodruff, *Adv. Funct. Mater.* **2024**, 2313092.
- [41] H. Xu, L. Du, *Curr. Opin. Biomed. Eng.* **2023**, *27*, 100464.
- [42] A. C. Abdullah, O. Ozarslan, S. S. Farshi, S. R. Dabbagh, *Aggregate* **2024**, <https://doi.org/10.1002/agt2.495>.
- [43] P. Mieszczanek, T. M. Robinson, P. D. Dalton, D. W. Huttmacher, *Adv. Mater.* **2021**, *33*, 2100519.
- [44] R. S. Diaz, E. M. De-Juan-Pardo, P. D. Dalton, T. R. Dargaville, *Macromol. Mater. Eng.* **2023**, *308*, 8.
- [45] F. M. Wunner, S. Eggert, J. Maartens, O. Bas, P. D. Dalton, E. M. De-Juan-Pardo, D. W. Huttmacher, *Addit. Manuf.* **2019**, *6*, 90.
- [46] J. C. Kade, P. D. Dalton, *Adv. Healthcare Mater.* **2021**, *10*, 2001232.
- [47] H. Xu, I. Liashenko, A. Lucchetti, L. Du, Y. Dong, D. Zhao, J. Meng, H. Yamane, P. D. Dalton, *Adv. Mater. Technol.* **2022**, *7*, 8.
- [48] C. Böhm, P. Stahlhut, J. Weichhold, A. Hrynevich, J. Teßmar, P. D. Dalton, *Small* **2022**, *18*, 7.
- [49] M. Gwiazda, S. Kumar, W. Świeszkowski, S. Ivanovski, C. Vaquette, *J. Mech. Behav. Biomed. Mater.* **2019**, *104*, 103631.
- [50] M. Castilho, D. Feyen, M. Flandes-Iparraguirre, G. Hochleitner, J. Groll, P. A. F. Doevendans, T. Vermonden, K. Ito, J. P. G. Sluijter, J. Malda, *Adv. Healthcare Mater.* **2017**, *6*, 1700311.
- [51] J. Uribe-Gomez, A. Posada-Murcia, A. Shukla, M. Ergin, G. Constante, I. Apsite, D. Martin, M. Schwarzer, A. Caspari, A. Snytnska, S. Salehi, L. Ionov, *ACS Appl. Bio Mater.* **2021**, *4*, 1720.

- [52] G. Hochleitner, J. F. Hümmer, R. Luxenhofer, J. Groll, *Polymer* **2014**, *55*, 5017.
- [53] B. Zhang, B. Seong, V. D. Nguyen, D. Byun, J. *Micromech. Microeng.* **2016**, *26*, 025015.
- [54] J. Meng, F. Boschetto, S. Yagi, E. Marin, T. Adachi, X. Chen, G. Pezzotti, S. Sakurai, S. Sasaki, T. Aoki, H. Yamane, H. Xu, *Biomater. Adv.* **2022**, *135*, 112686.
- [55] J. Meng, F. Boschetto, S. Yagi, E. Marin, T. Adachi, X. Chen, G. Pezzotti, S. Sakurai, H. Yamane, H. Xu, *Mater. Des.* **2022**, *219*, 110781.
- [56] G. Hochleitner, M. Kessler, M. Schmitz, A. R. Boccaccini, J. Teßmar, J. Groll, *Mater. Lett.* **2017**, *205*, 257.
- [57] J. Meng, F. Boschetto, S. Yagi, E. Marin, T. Adachi, X. Chen, G. Pezzotti, S. Sakurai, H. Yamane, H. Xu, *Mater. Des.* **2021**, *210*, 110063.
- [58] R. Sanchez Diaz, J. R. Park, L. L. Rodrigues, P. D. Dalton, E. M. De-Juan-Pardo, T. R. Dargaville, *Adv. Mater. Technol.* **2022**, *7*, 2100508.
- [59] C. Böhm, B. Tandon, A. Hrynevich, J. Teßmar, P. D. Dalton, *Macromol. Chem. Phys.* **2022**, *223*, 2100417.
- [60] S. Ashour, L. Du, X. Zhang, S. Sakurai, H. Xu, *Eur. Polym. J.* **2023**, *204*, 112675.
- [61] F. Chen, G. Hochleitner, T. Woodfield, J. Groll, P. D. Dalton, B. G. Amsden, *Biomacromolecules* **2016**, *17*, 214.
- [62] G. Hochleitner, F. Chen, C. Blum, P. D. Dalton, B. Amsden, J. Groll, *Acta Biomater.* **2018**, *72*, 110.
- [63] N. Pien, M. Bartolf-Kopp, L. Parmentier, J. Delaey, L. De Vos, D. Mantovani, S. Van Vlierberghe, P. Dubruel, T. Jungst, *Macromol. Mater. Eng.* **2022**, *307*, 15.
- [64] A. Daneshfar, L. F. Dumée, T. C. Hughes, L. Kong, *Addit. Manuf.* **2022**, *51*, 102623.
- [65] D. Nahm, F. Weigl, N. Schaefer, A. Sancho, A. Frank, J. Groll, C. Villmann, H. W. Schmidt, P. D. Dalton, R. Luxenhofer, *Mater. Horiz.* **2020**, *7*, 928.
- [66] A. Nadernezhad, M. Ryma, H. Genç, I. Cicha, T. Jüngst, J. Groll, *Adv. Mater. Technol.* **2021**, *6*, 2100221.
- [67] J. N. Haigh, T. R. Dargaville, P. D. Dalton, *Mater. Sci. Eng. C* **2017**, *77*, 883.
- [68] G. Hochleitner, E. Fürsattel, R. Giesa, J. Groll, H. W. Schmidt, P. D. Dalton, *Macromol. Rapid Commun.* **2018**, *39*, 1800055.
- [69] J. Mechau, A. Frank, E. Bakirci, S. Gumbel, T. Jungst, R. Giesa, J. Groll, P. D. Dalton, H. W. Schmidt, *Macromol. Chem. Phys.* **2021**, *222*.
- [70] J. C. Kade, B. Tandon, J. Weichhold, D. Pisignano, L. Persano, R. Luxenhofer, P. D. Dalton, *Polym. Int.* **2021**, *70*, 1725.
- [71] N. C. Paxton, S. Luposchinsky, A. Reizabal, P. G. Saiz, S. Bade, M. A. Woodruff, P. D. Dalton, *Adv. Mater. Technol.* **2023**, *9*, 2301190.
- [72] A. Reizabal, B. L. Devlin, N. C. Paxton, P. G. Saiz, I. Liaschenko, S. Luposchinsky, M. A. Woodruff, S. L. Mendez, P. D. Dalton, *Macromol. Rapid Commun.* **2023**, *44*, 2300424.
- [73] Z. Shao, H. Chen, Q. Wang, G. Kang, J. Jiang, X. Wang, W. Li, Y. Liu, G. Zheng, *IEEE Sens. J.* **2022**, *22*, 18560.
- [74] G. Constante, I. Apsite, P. Auerbach, S. Aland, D. Schönfeld, T. Pretsch, P. Milkin, L. Ionov, *ACS Appl. Mater. Interfaces* **2022**, *14*, 20208.
- [75] G. Constante, I. Apsite, D. Schönfeld, T. Pretsch, L. Ionov, *Small Struct.* **2023**, *4*, 2300040.
- [76] D. C. S. Costa, P. D. C. Costa, M. C. Gomes, A. Chandrakar, P. A. Wieringa, L. Moroni, J. F. Mano, *ACS Mater. Lett.* **2022**, *4*, 701.
- [77] S. Florczak, T. Lorson, T. Zheng, M. Mrlik, D. W. Huttmacher, M. J. Higgins, R. Luxenhofer, P. D. Dalton, *Polym. Int.* **2019**, *68*, 735.
- [78] S. Luposchinsky, S. Jörissen, A. Nüchter, P. D. Dalton, *Macromol. Mater. Eng.* **2022**, *307*, 6.
- [79] M. Shahverdi, S. Seifi, A. Akbari, K. Mohammadi, A. Shamloo, M. R. Movahhedy, *Sci. Rep.* **2022**, *12*, 16.
- [80] A. Reizabal, P. G. Saiz, S. Luposchinsky, I. Liaschenko, D. S. Chasko, S. Lanceros-Méndez, G. Lindberg, P. D. Dalton, *ACS Biomater. Sci. Eng.* **2023**, *10*, 1843.
- [81] T. D. Brown, A. Slotosch, L. Thibaudeau, A. Taubenberger, D. Loessner, C. Vaquette, P. D. Dalton, D. W. Huttmacher, *Biointerphases* **2012**, *7*, 16.
- [82] A. Abdal-hay, N. Abbasi, M. Gwiazda, S. Hamlet, S. Ivanovski, *Eur. Polym. J.* **2018**, *105*, 257.
- [83] L. Du, L. Yang, B. Xu, L. Nie, H. Lu, J. Wu, H. Xu, Y. Lou, *New J. Chem.* **2022**, *46*, 13565.
- [84] X. Qu, P. Xia, J. He, D. Li, *Mater. Lett.* **2016**, *185*, 554.
- [85] E. Hewitt, S. Mros, M. McConnell, J. D. Cabral, A. Ali, *Biomed. Mater.* **2019**, *14*, 055013.
- [86] F. Afghah, N. B. Iyison, A. Nadernezhad, A. Midi, O. Sen, B. Saner Okan, M. Culha, B. Koc, *Adv. Healthcare Mater.* **2022**, *11*, 16.
- [87] N. C. Paxton, J. Ren, M. J. Ainsworth, A. K. Solanki, J. R. Jones, M. C. Allenby, M. M. Stevens, M. A. Woodruff, *Macromol. Rapid Commun.* **2019**, *40*, 6.
- [88] S. Mansi, S. V. Dummert, G. J. Topping, M. Z. Hussain, C. Rickert, K. M. A. Mueller, T. Kratky, M. Elsner, A. Casini, F. Schilling, R. A. Fischer, O. Lieleg, P. Mela, *Adv. Funct. Mater.* **2023**, *34*, 2304907.
- [89] E. Pickering, N. C. Paxton, A. Bo, B. O'Connell, M. King, M. A. Woodruff, *Adv. Eng. Mater.* **2022**, *11*, 24.
- [90] N. Golafshan, M. Castilho, A. Daghrely, M. Alehosseini, T. van de Kemp, K. Krikonis, M. de Ruijter, R. Dal-Fabbro, A. Dolatshahipirouz, S. B. Bhaduri, M. C. Bottino, J. Malda, *ACS Appl. Mater. Interfaces* **2022**, *15*, 12735.
- [91] L. Pang, N. C. Paxton, J. Ren, F. Liu, H. Zhan, M. A. Woodruff, A. Bo, Y. Gu, *ACS Appl. Mater. Interfaces* **2020**, *12*, 47993.
- [92] K. Somszor, O. Bas, F. Karimi, T. Shabab, N. T. Saidy, A. J. O'Connor, A. V. Ellis, D. Huttmacher, D. E. Heath, *ACS Macro Lett.* **2020**, *9*, 1732.
- [93] J. H. Y. Chung, S. Sayyar, G. G. Wallace, *Polymers* **2022**, *14*, 319.
- [94] Z. Meng, J. He, Z. Xia, D. Li, *Mater. Lett.* **2020**, *278*, 128440.
- [95] X. Wu, T. Vedelaar, R. Li, R. Schirhagl, M. Kamperman, M. K. Włodarczyk-Biegun, *Int. J. Bioprint.* **2023**, *32*, e00288.
- [96] K. M. A. Mueller, G. J. Topping, S. P. Schwaminger, Y. Zou, D. M. Rojas-González, E. M. De-Juan-Pardo, S. Berensmeier, F. Schilling, P. Mela, *Biomater. Sci.* **2021**, *9*, 4607.
- [97] P. G. Saiz, A. Reizabal, J. L. Vilas-vilela, S. Lanceros-mendez, P. D. Dalton, *ACS Appl. Polym. Mater.* **2023**, *5*, 3883.
- [98] J. C. Kade, E. Bakirci, B. Tandon, D. Gorgol, M. Mrlik, R. Luxenhofer, P. D. Dalton, *Macromol. Mater. Eng.* **2022**, *307*, 8.
- [99] G. Cedillo-Servin, J. M. Ouafa Dahri, J. V. Duijn, J. S. Fanny Sage, F. D. M. André Pereira, J. Malda, N. Geijsen, A. M. Pinto, M. Castilho, *Small* **2023**, 2307178.
- [100] P. G. Saiz, A. Reizabal, S. Luposchinsky, J. L. Vilas-Vilela, S. Lanceros-Mendez, P. D. Dalton, *Adv. Mater. Technol.* **2023**, *8*, 2202063.
- [101] M. Mirzaei, G. Dodi, I. Gardikiotis, S.-A. Pasca, S. Mirdamadi, G. Subr, C. Echalié, C. Puel, R. Morent, R. Ghobeira, N. Soleymanzadeh, M. Moser, S. Goriel, A. Shavandi, *Biomater. Adv.* **2022**, *149*, 213361.
- [102] Y. Su, Y. Zhang, Y. Chen, S. S. Majidi, M. Dong, M. Chen, *Mater. Today Phys.* **2024**, *41*, 101344.
- [103] T. He, Z. Wang, F. Zhong, H. Fang, P. Wang, W. Hu, *Adv. Mater. Technol.* **2019**, *4*, 18.
- [104] M. L. Muerza-Cascante, A. Shokoohmand, K. Khosrotehrani, D. Haylock, P. D. Dalton, D. W. Huttmacher, D. Loessner, *Acta Biomater.* **2017**, *52*, 145.
- [105] M. J. Ainsworth, O. Lotz, A. Gilmour, A. Zhang, M. J. Chen, D. R. McKenzie, M. M. M. Bilek, J. Malda, B. Akhavan, M. Castilho, *Adv. Funct. Mater.* **2023**, *33*, 2206583.

- [106] A. Hammerl, C. E. Diaz Cano, E. M. De-Juan-Pardo, M. van Griensven, P. S. P. Poh, *Int. J. Mol. Sci.* **2019**, *20*, 1068.
- [107] N. Abbasi, A. Abdal-Hay, S. Hamlet, E. Graham, S. Ivanovski, *ACS Biomater. Sci. Eng.* **2019**, *5*, 3448.
- [108] A. Farag, A. Abdal-hay, P. Han, S. Ivanovski, *Ceram. Int.* **2022**, *49*, 8015.
- [109] Y. Su, C. A. Müller, X. Xiong, M. Dong, M. Chen, *Nano Lett.* **2022**, *22*, 3583.
- [110] A. Mathew, B. L. Devlin, D. Singh, N. C. Paxton, M. A. Woodruff, *Macromol. Mater. Eng.* **2023**, *10*, 2300168.
- [111] S. Bertlein, G. Hochleitner, M. Schmitz, J. Tessmar, M. Raghunath, P. D. Dalton, J. Groll, *Adv. Healthcare Mater.* **2019**, *8*, 1801544.
- [112] B. N. Jensen, Y. Wang, A. Le Friec, S. Nabavi, M. Dong, D. Seliktar, M. Chen, *Npj Flex Electron* **2023**, *7*.
- [113] D. Olvera, M. Sohrabi Molina, G. Hendy, M. G. Monaghan, *Adv. Funct. Mater.* **2020**, *30*, 1909880.
- [114] Y. Zhang, A. Le Friec, D. Sun, M. Chen, *Chem. Eng. J.* **2022**, *455*, 140555.
- [115] Y. Wang, Y. Zhang, Z. Zhang, Y. Su, Z. Wang, M. Dong, M. Chen, *Colloids Surf., B* **2020**, *195*, 111210.
- [116] J. Li, P. Hashemi, T. Liu, K. M. Dang, M. G. K. Brunk, X. Mu, A. S. Nia, W. D. Sacher, X. Feng, J. K. S. Poon, *bioRxiv* **2023**, 08.
- [117] I. Unalan, I. Occhipinti, M. Miola, E. Vernè, A. R. Boccaccini, *Macromol. Biosci.* **2023**, *14*, 2300397.
- [118] J. N. Haigh, Y. M. Chuang, B. Farrugia, R. Hoogenboom, P. D. Dalton, T. R. Dargaville, *Macromol. Rapid Commun.* **2016**, *37*, 93.
- [119] S. Wang, M. Sarwat, P. Wang, D. C. Surrao, D. G. Harkin, J. A. St John, E. C. L. Bolle, A. Forget, P. D. Dalton, T. R. Dargaville, *Macromol. Rapid Commun.* **2020**, *41*, 2000295.
- [120] E. I. Liu, E. Footner, A. Quigley, C. Baker, P. Foley, E. Pirogova, R. M. I. Kapsa, C. D. O'Connell, *Macromol. Mater. Eng.* **2023**, *11*, 2300042.
- [121] J. Zeng, H. Wang, Y. Lin, J. Zhang, F. Liang, F. Fang, F. Yang, P. Wang, Z. Zhu, X. Chen, X. Chen, Z. Wang, N. Cai, Y. Tang, P. Wu, *Microfluidics Nanofluidics* **2018**, *22*, 10.
- [122] M. Ryma, H. Genc, A. Nadernezhad, I. Paulus, D. Schneiderreit, O. Friedrich, K. Andelovic, S. Lyer, C. Alexiou, I. Cicha, J. Groll, *Adv. Mater.* **2022**, *34*, 2200653.
- [123] J. Visser, F. P. W. Melchels, J. E. Jeon, E. M. Van Bussel, L. S. Kimpton, H. M. Byrne, W. J. A. Dhert, P. D. Dalton, D. W. Hutmacher, J. Malda, *Nat. Commun.* **2015**, *6*, 10.
- [124] O. Bas, E. M. De-Juan-Pardo, M. P. Chhaya, F. M. Wunner, J. E. Jeon, T. J. Klein, D. W. Hutmacher, *Eur. Polym. J.* **2015**, *72*, 451.
- [125] O. Bas, E. M. De-Juan-Pardo, C. Meinert, D. D'Angella, J. G. Baldwin, L. J. Bray, R. M. Wellard, S. Kollmannsberger, E. Rank, C. Werner, T. J. Klein, I. Catelas, D. W. Hutmacher, *Biofabrication* **2017**, *9*, 025014.
- [126] N. T. Saïdy, A. Fernández-Colino, B. S. Heidari, R. Kent, M. Vernon, O. Bas, S. Mulderrig, A. Lubig, J. C. Rodríguez-Cabello, B. Doyle, D. W. Hutmacher, E. M. De-Juan-Pardo, P. Mela, *Adv. Funct. Mater.* **2022**, *21*, 32.
- [127] T. Jungst, I. Pennings, M. Schmitz, A. J. W. P. Rosenberg, J. Groll, D. Gawlitta, *Adv. Funct. Mater.* **2019**, *29*, 1905987.
- [128] T. Xu, J. Gu, J. Meng, L. Du, A. Kumar, H. Xu, *J. Mech. Behav. Biomed. Mater.* **2022**, *132*, 105277.
- [129] L. Du, Y. Xu, H. Xu, X. Ye, Y. Li, *Colloids Surf., A* **2022**, *200*, 641.
- [130] G. Zhang, Y. Xu, Y. Sun, X. Ye, L. Du, H. Xu, *Langmuir* **2023**, *39*, 7891.
- [131] M. de Ruijter, A. Ribeiro, I. Dokter, M. Castilho, J. Malda, *Adv. Healthcare Mater.* **2019**, *8*, 1800418.
- [132] M. J. Ainsworth, N. Chirico, M. Ruijter, A. Hrynevich, I. Dokter, J. P. G. Sluijter, J. Malda, A. Mil, M. Castilho, *Biofabrication* **2023**, *15*, 035025.
- [133] G. Constante, I. Apsite, H. Alkhamis, M. Dulle, M. Schwarzer, A. Caspari, A. Synytska, S. Salehi, L. Ionov, *ACS Appl. Mater. Interfaces* **2021**, *13*, 12767.
- [134] D. Kilian, M. von Witzleben, M. Lanaro, C. S. Wong, C. Vater, A. Lode, M. C. Allenby, M. A. Woodruff, M. Gelinsky, *J. Funct. Biomater.* **2022**, *13*, 75.
- [135] Y. Jin, C. Xie, Q. Gao, X. Zhou, G. Li, J. Du, Y. He, *Mater. Des.* **2021**, *197*, 109277.
- [136] A. Dufour, X. B. Gallostra, C. O'Keeffe, K. Eichholz, S. Von Euw, O. Garcia, D. J. Kelly, *Biomaterials* **2022**, *283*, 121405.
- [137] G. Größbacher, M. Bartolf-Kopp, C. Gergely, P. N. Bernal, S. Florczak, M. Ruijter, N. G. Rodriguez, J. Groll, J. Malda, T. Jungst, R. Levato, *Adv. Mater.* **2023**, *35*, 2300756.
- [138] X. Barceló, K. F. Eichholz, I. F. Gonçalves, O. Garcia, D. J. Kelly, *Acta Biomater.* **2023**, *158*, 216.



Paula G. Saiz is a Margarita Salas post-doctoral researcher at the University of the Basque Country (UPV/EHU). She holds a Physics degree from the University of Cantabria and a Ph.D. in Materials Science and Technology from the UPV/EHU. Her doctoral research focused on the development of advanced materials and sensors for environmental pollutants detection and removal. Currently, as a postdoctoral researcher, she is exploring the potential of melt electrowriting for novel materials processing and its applicability across diverse fields.



Ander Reizabal, a post-doctoral researcher at the Basque Center for Materials, Applications, and Nanostructures (BCMaterials), holds a degree in Environmental Sciences and a Ph.D. in Materials Science and Technology from the University of the Basque Country. His focus lies in driving innovation in materials and promoting process sustainability for advanced applications. Recently, he has ventured into exploring additive manufacturing technologies, with a special emphasis on electrohydrodynamic 3D printing.



Jose Luis Vilas-Vilela is an associate professor in physical chemistry at the University of the Basque Country, where he leads the Macromolecular Chemistry Group. He has participated in numerous research projects, related to the synthesis and processing of polymeric materials. His current research interest includes the synthesis and characterization of polymers and composite materials with functional properties, the development of biocompatible polymers and polymers from renewable sources, and the 3D printing of all these materials.



Paul Dalton is the Bradshaw and Holzapfel Research Professor in Transformational Science and Mathematics at the Phil and Penny Knight Campus for Accelerating Scientific Impact at the University of Oregon. An early adopter of melt electrospinning and pioneer of melt electrowriting, his research focuses on processes and biomaterials that can be translated to the clinic. His academic career is especially international and multidisciplinary, with over 25 years of experience across various fields. Currently, his team specializes in pushing the boundaries of new biomedical manufacturing technologies, particularly melt electrowriting, as well as the development of affordable open-source devices.



Senentxu Lanceros-Mendez is an Ikerbasque Professor and scientific director at the Basque Center for Materials, Applications and Nanostructures (BCMaterials). He is also associate professor at the Physics Department of the University of Minho (on leave). He graduated in Physics at the University of the Basque Country, and obtained his doctoral degree at the Institute of Physics at Julius-Maximilians Universität Würzburg (Germany). His research is focused on the development of smart and multifunctional materials for sensors and actuators, energy, environmental, and biomedical applications, showcasing a comprehensive and impactful scientific endeavor.